

# Nemchinov-Dyson Solutions of the 2D Axisymmetric Inviscid Compressible Flow Equations

Jesse F. Giron,<sup>1,2,\*</sup> Scott D. Ramsey,<sup>1,†</sup> and Roy S. Baty<sup>1,‡</sup>

<sup>1</sup>*Applied Physics, Los Alamos National Laboratory,  
P.O. Box 1663, MS T082, Los Alamos, New Mexico 87545*

<sup>2</sup>*Department of Physics, Box 871504, Arizona State University, Tempe, Arizona 85287-1504*  
(Dated: October, 2020)

We investigate the 2D inviscid compressible flow equations in axisymmetric coordinates, constrained by an ideal gas equation of state (EOS). Beginning with the assumption that the 2D velocity field is space-time separable and linearly variable in each corresponding spatial coordinate, we proceed to derive an infinite family of elliptic or hyperbolic, uniformly expanding or contracting “gas cloud” solutions. Construction of specific example solutions belonging to this family is dependent on the solution of a system of nonlinear, coupled, second-order ordinary differential equations, and the prescription of an additional physical process of interest (e.g., uniform temperature or uniform entropy flow). The physical and computational implications of these solutions as pertaining to quantitative code verification or model qualification studies are discussed in some detail.

Keywords: hydrodynamics, Euler equations, self-similar solutions

## I. INTRODUCTION

A classical family of self-similar solutions of the one-dimensional (1D) inviscid compressible flow (Euler) equations for an ideal gas involves the “unsteady motion of a gas when the velocity is proportional to distance from the center of symmetry,” as originally investigated by Sedov [1] (see also Zel’dovich *et al* [2], Cantwell [3], and Atzeni *et al* [4]). As discussed in rigorous detail by Sedov [1], these “linear velocity” solutions are intimately connected to a variety of other important inviscid compressible flow patterns, including

“...the problem of propagation of a detonation wave in a medium with variable density ... the problem of an intense explosion ... and the problem of an intense point explosion in a medium with variable initial density...”

and, perhaps disseminated most widely, the adiabatic expansion of gas clouds [5, 6]. These solutions have found extensive practical applications in the fields of plasma physics as shown by Motz [7] and Pert [8, 9] (and references therein), astrophysical modeling (e.g., the expansion of supernova remnants [5]), and the evaluation of inertial confinement fusion concepts [4, 7, 10–18]. In addition to their physical applications, some of the Kidder [10–12] and Coggeshall [15–17] solutions have also more recently been exercised as test problems for the quantitative verification of inviscid compressible flow codes [19–22].

In all of these contexts, and consistent with the nature of both the model verification and model qualification

processes as defined by Oberkampf *et al* [23], establishing the practical utility of mathematical models (as exemplified by their sufficient fidelity and predictive capability within applications of interest) demands an iterative process wherein those models are refined and improved as necessary. This notion in turn often motivates an ever-accelerating need for new surrogate problems to be used in conjunction with, for example, computational science codes of relevance to any of the aforementioned physical applications.

Against this broader backdrop, the 1D inviscid Euler equations for an ideal gas thus represent a natural starting point for the exploration of a wider variety of flow scenarios with relevance to the aforementioned applications. Along these lines, possible modifications of the 1D inviscid Euler equations include but are not necessarily limited to the inclusion of non-ideal material constitutive laws, multi-fluid representations, charged particle transport phenomena, reaction-transport processes, relativistic effects, gravitational, electromagnetic, or thermal radiation field coupling, or higher-fidelity geometric effects such as two and three-dimensional (2D and 3D, respectively) representations in various coordinate systems. Among these and many other possible choices, multi-dimensional generalizations of the 1D linear velocity flows form the basis of this study.

An essential entry point into multi-dimensional fluid flows is Chandrasekhar’s [24] summary and thorough codification of the celebrated “ellipsoidal figures of equilibrium.” Intimately related to these scenarios is the extensive body of literature pertaining to ellipsoidal gas clouds; see, for example, Ovsyannikov [25, 26], Nemchinov [27], Anisimov *et al* [28], Dyson [29, 30], Hara *et al* [31], Tarasova [32], Shieh [33], Rogers *et al* [34], and Gaffet [35–41]. All these studies feature multi-dimensional fluid bodies that are contracting, expanding, or rotating under various ancillary assumptions. Some of these scenarios also feature the linear velocity assumption

\* jgiron@lanl.gov; jfgiron@asu.edu

† ramsey@lanl.gov

‡ rbaty@lanl.gov

applied in multiple dimensions, which despite its simplicity maintains a profound physical significance. As noted by Gaffet[35–41],

“The physical motivation for considering the simplifying assumption ... on the form of the velocity field, lies essentially in the fact that the basic kinematical quantity, the deformation tensor ... is then uniformly distributed throughout space. That assumption ... may be viewed as a natural generalization of the rigid flows that obtain when the uniform value of the deformation tensor vanishes...”

and by Shieh [33],

“Those who are not familiar with this field often get a misleading impression ... that only trivial results can follow from such a simplifying assumption. ... Now, the assumption ... adds internal vortex motion as well as the pulsation of the semiaxes into the study of the problem. Furthermore, [it] contains the interactions of these types of motion. Even with the aid of modern computers, these interactions are not yet fully explored...”

thus further motivating this study.

Within the tremendous body of work pertaining to ellipsoidal gas cloud motion, the simplest generalizations to multi-dimensional geometries of the 1D linear velocity solutions appear to have been originated independently by Ovsyannikov [25, 26] and Dyson [29, 30]. Both these models feature compressible fluid ellipsoids in the absence of any dissipative or otherwise ancillary effects, and so are associated with the multi-dimensional inviscid Euler equations for an ideal gas. As noted by Dyson [29, 30], the objective of these formulations is to find “... a model which will describe the free expansion of a non-spherical cloud of gas into a vacuum.” Commensurate with this objective, both Nemchinov [27] (specializing Ovsyannikov’s [25, 26] more general results) and Dyson [29, 30] proceed under the additional assumptions of

1. Three-dimensional (3D) geometry in a Cartesian coordinate system,
2. The gas cloud motion is irrotational,
3. The gas cloud expands by a uniform change of scale in each spatial coordinate (i.e., the linear velocity assumption),
4. The expansion proceeds with spatially uniform temperature, leading to a Gaussian form of the cloud mass density distribution (Nemchinov [27] also presents a case where this assumption is replaced with a quadratic temperature distribution),

the aggregate result of which is the establishment of a fluid flow scenario that will hereafter be referred to as the 3D Cartesian “Nemchinov-Dyson problem” for the sake of brevity, and also for some degree of consistency with the existing literature on the subject<sup>1</sup>.

Both Nemchinov [27] and Dyson [29, 30] provide some numerical solutions for their models. Deeper analytical studies of the 3D Cartesian Nemchinov-Dyson problem are provided by both Anisimov *et al* [28] and Gaffet [35–41]. In particular, Anisimov *et al* [28] show for an ideal gas without inner degrees of freedom, the 3D Cartesian Nemchinov-Dyson problem may be solved analytically in terms of elliptic integral functions of the third kind. A later and more detailed analysis along the same lines is provided in two studies by Gaffet [35–41]: both also feature the key assumption of a monoatomic polytropic gas, thus leading to solutions of the 3D Cartesian Nemchinov-Dyson problem in terms of quadratures (of which the elliptic integral representations are a special case).

Also exemplified by Dyson, the notions of symmetries and associated conserved quantities play an important role in the construction of both Anisimov *et al* [28] and Gaffet’s [35–41] analytical solutions. This correspondence also explicitly appears in related studies by Coggeshall [15–17], who encodes the salient mathematics in the theory of invariance under groups of continuous point transformations (Lie groups). Using this systematic group-theoretic or symmetry analysis formalism, Coggeshall [15–17] derives numerous new analytical solutions to the multi-dimensional inviscid Euler equations, including rotational and irrotational linear velocity instantiations in the 2D axisymmetric, 2D cylindrical, and 3D spherical coordinate systems. These analytical results bear close resemblance to solutions of the 3D Cartesian Nemchinov-Dyson problem established through other, but related means.

Despite the voluminous amount of work performed to date on the subject of expanding ellipsoidal gas clouds, there exist numerous additional opportunities for the development and codification of new Nemchinov-Dyson and related solutions. In particular, some limitations of existing solutions include but are not necessarily limited to:

- Representation within the 3D Cartesian coordinate system. Representations in other 2D and 3D coordinate systems have yet to be widely explored, aside from their appearance in Coggeshall’s [15–17] work.
- Most scenarios considered to date have only featured adiabatic expansion processes. Certain adiabatic compression or cumulation scenarios (see, for

<sup>1</sup> An equally legitimate moniker for this scenario is the 3D Cartesian “irrotational Ovsyannikov-Dyson problem,” in light of Ovsyannikov’s seminal contributions to the more general scenario featuring rotation as well as expansion. Dyson independently treated both the rotational case and its irrotational sub-case.

example, Sedov [1], Atzeni *et al* [4], or Ramsey [42]) - and the associated modification of ellipsoidal figures to alternate hyperconic section surfaces - have been less thoroughly explored.

- The isothermal or Gaussian density instantiations have been subject to the most extensive investigation, as have uniform entropy and parabolic temperature solutions. Commensurate with this degree of freedom, there exists an ostensibly infinite variety of alternate solution realizations.

The motivation behind this work is thus to leverage the existing developments in Nemchinov-Dyson and multi-dimensional Coggeshall [15–17] problems to obtain and analyze a variety of new but related analytical or semi-analytical solutions in additional coordinate systems, for adiabatic implosion scenarios, and featuring alternate spatial flow patterns. Any new solutions derived in this program of study will therefore be available for further analysis from the standpoint of symmetry analysis theory (see for example Coggeshall [15–17, 43, 44], Giron *et al* [45], or McHardy *et al* [46]), or for integration within code verification or model qualification practices for the assessment of multi-dimensional inviscid compressible flow codes.

In support of these goals, Sec. II provides an overview of the relevant mathematical model, including certain assumptions and results surrounding the assumed multi-dimensional geometry and equation of state constitutive law. A formalized definition of a generalized Nemchinov-Dyson problem for use throughout the remainder of this study is provided in Sec. III, followed by derivation and analysis of some possible solution archetypes. Several detailed example solutions obtained via this formalism are presented in Sec. IV. Finally, we conclude and provide recommendations for future study in Sec. V.

## II. MATHEMATICAL MODEL

As shown by many authors (for example, Harlow and Amsden [47]), the inviscid compressible flow (Euler) equations in a general coordinate system are as follows:

$$\frac{\partial \rho}{\partial t} + (\vec{u} \cdot \vec{\nabla}) \rho + \rho (\vec{\nabla} \cdot \vec{u}) = 0, \quad (1)$$

$$\frac{\partial \vec{u}}{\partial t} + (\vec{u} \cdot \vec{\nabla}) \vec{u} + \frac{1}{\rho} \vec{\nabla} P = 0, \quad (2)$$

$$\frac{\partial E}{\partial t} + (\vec{u} \cdot \vec{\nabla}) E + \frac{1}{\rho} \vec{\nabla} \cdot (P \vec{u}) = 0, \quad (3)$$

where the mass density  $\rho(\vec{r}, t)$ , bulk flow velocity vector  $\vec{u}(\vec{r}, t)$ , pressure  $P(\vec{r}, t)$ , and total energy per unit mass  $E(\vec{r}, t)$  are functions of the position vector  $\vec{r}$  and time  $t$ . The total energy per unit mass may be further decomposed into the specific internal energy  $I(\vec{r}, t)$  (SIE; internal energy per unit mass) and specific kinetic energy,

that is

$$E(\vec{r}, t) = I(\vec{r}, t) + \frac{1}{2} \vec{u}(\vec{r}, t) \cdot \vec{u}(\vec{r}, t). \quad (4)$$

Conservation of mass, momentum and energy are represented by Eqs. (1)-(3), respectively. Equation (3) may be rewritten, using Eqs. (1), (2), and (4), as

$$\frac{\partial I}{\partial t} + (\vec{u} \cdot \vec{\nabla}) I - \frac{P}{\rho^2} \left[ \frac{\partial \rho}{\partial t} + (\vec{u} \cdot \vec{\nabla}) \rho \right] = 0. \quad (5)$$

Equation (5) may be further reduced using the fundamental thermodynamic relation [48–52] between  $\rho$ ,  $P$ ,  $I$ , the fluid temperature  $T$ , and the fluid entropy  $S$ ; that is,

$$dI = T dS + \frac{P}{\rho^2} d\rho. \quad (6)$$

Using the chain rule and Eq. (6), Eq. (5) becomes

$$\frac{\partial S}{\partial t} + (\vec{u} \cdot \vec{\nabla}) S = 0, \quad (7)$$

also known as the equation for isentropic flow. Equation (7) is expected to result from Eqs. (1)-(3) since they do not feature dissipative processes such as viscosity or heat conduction. Moreover, if the fluid entropy  $S$  is assumed to be a function of the fluid density  $\rho$  and pressure  $P$ , then Eq. (7) may be expanded to yield

$$\left. \frac{\partial S}{\partial \rho} \right|_P \left[ \frac{\partial \rho}{\partial t} + (\vec{u} \cdot \vec{\nabla}) \rho \right] + \left. \frac{\partial S}{\partial P} \right|_\rho \left[ \frac{\partial P}{\partial t} + (\vec{u} \cdot \vec{\nabla}) P \right] = 0. \quad (8)$$

Substituting Eq. (1) into Eq. (8), we find

$$\frac{\partial P}{\partial t} + (\vec{u} \cdot \vec{\nabla}) P + K_S (\vec{\nabla} \cdot \vec{u}) = 0, \quad (9)$$

where  $K_S(\rho, P)$  is the adiabatic bulk modulus, which is defined by

$$K_S(\rho, P) \equiv -\rho \left. \frac{\partial S}{\partial \rho} \right|_P, \quad (10)$$

or as shown by Axford [53],

$$K_S(\rho, P) = \frac{P}{\rho} \left. \frac{\partial P}{\partial I} \right|_\rho + \rho \left. \frac{\partial P}{\partial \rho} \right|_I. \quad (11)$$

The adiabatic bulk modulus appears only in the total energy (or entropy) conservation relation given by Eq. (9), and is a measure of the fluid's resistance to uniform, constant entropy compression. It is also related to the local fluid sound speed  $c$  by

$$K_S = \rho c^2. \quad (12)$$



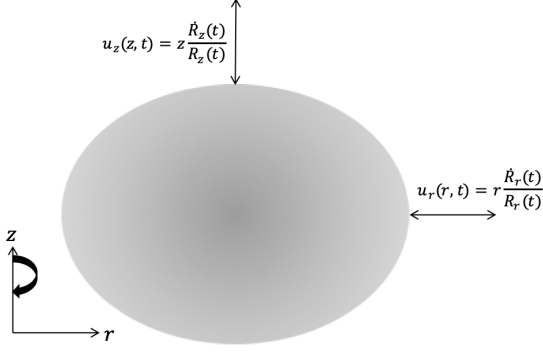


FIG. 2 Notional depiction of the Nemchinov-Dyson problem. The ideal gas cloud (depicted here as an ellipse for ease of illustration) has an arbitrary eccentricity and interior state distribution at  $t = 0$ , with Eqs. (28) and (29) representing the flow velocities throughout [where the scale velocities  $\dot{R}_r$  and  $\dot{R}_z$  may take on either positive or negative values]; otherwise there is no angular velocity associated with this configuration. The  $z$ -axis is the axis of rotation as shown by the curved arrow.

which may be solved using the method of characteristics to yield the associated form of the entropy as

$$S = S(P\rho^{-\gamma}), \quad (25)$$

where  $S$  is an arbitrary function of the indicated argument; for simplicity,  $S$  will be taken as uniform throughout the remainder of this work, such that, without loss of generality,

$$S = P\rho^{-\gamma}. \quad (26)$$

Using Eq. (23), Eqs. (15)-(17) remain unchanged while Eq. (18) finally becomes

$$\frac{\partial P}{\partial t} + u_r \frac{\partial P}{\partial r} + u_z \frac{\partial P}{\partial z} + \gamma P \left[ \frac{\partial u_r}{\partial r} + \frac{\partial u_z}{\partial z} + \frac{u_r}{r} \right] = 0 \quad (27)$$

Equations (15)-(17) and (27) are the inviscid Euler equations that will be used throughout the remainder of this study.

### III. THE NEMCHINOV-DYSON PROBLEM

As depicted in Fig. 2 and discussed extensively throughout Sec. I, a Nemchinov-Dyson solution of Eqs. (15)-(17) and (27) may be constructed by assuming separable, linear proportionalities between each of the featured flow velocity components and their associated spatial coordinates. In axisymmetric geometry, this assumption proceeds according to

$$u_r = r \frac{\dot{R}_r(t)}{R_r(t)}, \quad (28)$$

$$u_z = z \frac{\dot{R}_z(t)}{R_z(t)}, \quad (29)$$

where the “scale radii”  $R_r > 0$  and  $R_z > 0$  are functions of time to be determined, and the “scale velocities”  $\dot{R}_q$  ( $q \in r, z$ ) are defined by

$$\dot{R}_q \equiv \frac{dR_q}{dt}, \quad (30)$$

such that the overdots denote time differentiation.

Substituting Eqs. (28) and (29) into Eq. (15) yields

$$\frac{\partial \rho}{\partial t} + r \frac{\dot{R}_r}{R_r} \frac{\partial \rho}{\partial r} + z \frac{\dot{R}_z}{R_z} \frac{\partial \rho}{\partial z} + \rho \left( 2 \frac{\dot{R}_r}{R_r} + \frac{\dot{R}_z}{R_z} \right) = 0. \quad (31)$$

Using method of characteristics, we then find

$$\frac{dt}{1} = \frac{dr}{\frac{\dot{R}_r}{R_r} r} = \frac{dz}{\frac{\dot{R}_z}{R_z} z} = \frac{d\rho}{-\rho \left( 2 \frac{\dot{R}_r}{R_r} + \frac{\dot{R}_z}{R_z} \right)}, \quad (32)$$

or

$$\begin{aligned} \frac{\dot{R}_r}{R_r} dt &= \frac{dr}{r}, \\ \Rightarrow \xi(r, t) &= \frac{r}{R_r}, \end{aligned} \quad (33)$$

where  $\xi(r, t)$  is the constant of integration arising from the solution of the characteristic equation described in Eq. (33), that may otherwise be interpreted as a new variable in terms of which Eqs. (15)-(17) and (27) may be reformulated. Also from Eq. (32),

$$\begin{aligned} \frac{\dot{R}_z}{R_z} dt &= \frac{dz}{z}, \\ \Rightarrow \eta(z, t) &= \frac{z}{R_z}, \end{aligned} \quad (34)$$

where  $\eta(r, t)$  is the constant of integration arising from the solution of the characteristic equation described in Eq. (34), that again may otherwise be interpreted as another new variable in terms of which Eqs. (15)-(17) and (27) may be reformulated. Finally, we solve for  $d\rho$  and  $dt$  in Eq. (32) and find

$$\begin{aligned} \frac{d\rho}{\rho} &= - \left( 2 \frac{\dot{R}_r}{R_r} + \frac{\dot{R}_z}{R_z} \right) dt, \\ \Rightarrow \rho(r, z, t) &= \frac{1}{R_r^2 R_z} \Pi(\xi, \eta), \end{aligned} \quad (35)$$

thus yielding a solution for the Nemchinov-Dyson density  $\rho$  in terms of both the scale radii and  $\Pi$ , which is an arbitrary function of the arguments  $\xi$  and  $\eta$ .

We now substitute Eqs. (28), (29), and (33)-(35) into Eqs. (16) and (17) and find

$$\ddot{R}_r \xi + \frac{R_r^2 R_z}{R_r} \frac{1}{\Pi(\xi, \eta)} \frac{\partial P}{\partial \xi} = 0, \quad (36)$$

$$\ddot{R}_z \eta + \frac{R_r^2 R_z}{R_z} \frac{1}{\Pi(\xi, \eta)} \frac{\partial P}{\partial \eta} = 0, \quad (37)$$

respectively. Solving for the pressure  $P$  in both of the above equations then yields

$$P(r, z, t) = -\frac{\ddot{R}_r}{R_r R_z} \int \xi \Pi d\xi, \quad (38)$$

$$P(r, z, t) = -\frac{\ddot{R}_z}{R_r^2} \int \eta \Pi d\eta. \quad (39)$$

Furthermore, substituting Eqs. (28), (29), and (33)-(35) into Eq. (27) yields a third equation for the pressure  $P$ , namely,

$$\frac{\partial P}{\partial t} + r \frac{\dot{R}_r}{R_r} \frac{\partial P}{\partial r} + z \frac{\dot{R}_z}{R_z} \frac{\partial P}{\partial z} + \gamma P \left( 2 \frac{\dot{R}_r}{R_r} + \frac{\dot{R}_z}{R_z} \right) = 0, \quad (40)$$

which, using the same method of characteristics procedure as used to solve Eq. (31), has a solution given by

$$P(r, z, t) = \frac{1}{(R_r^2 R_z)^\gamma} \beta(\xi, \eta), \quad (41)$$

where  $\xi$  and  $\eta$  retain their previous definitions and, like the function  $\Pi$  appearing in the Nemchinov-Dyson density solution,  $\beta$  is an arbitrary function of the arguments  $\xi$  and  $\eta$ .

Since, on the grounds of physical realism, the pressure  $P$  must be a single-valued function, Eqs. (38), (39), and (41) yield the equivalences

$$\begin{aligned} \frac{1}{(R_r^2 R_z)^\gamma} \beta &= -\frac{\ddot{R}_z}{R_r^2} \int \eta \Pi d\eta \\ &= -\frac{\ddot{R}_r}{R_r R_z} \int \xi \Pi d\xi, \end{aligned} \quad (42)$$

or

$$-\frac{R_r^{1-2\gamma} R_z^{1-\gamma}}{\ddot{R}_r} = \frac{1}{\beta} \int \xi \Pi d\xi, \quad (43)$$

$$-\frac{R_r^{2-2\gamma} R_z^{-\gamma}}{\ddot{R}_z} = \frac{1}{\beta} \int \eta \Pi d\eta, \quad (44)$$

$$\frac{R_r \ddot{R}_r}{R_z \ddot{R}_z} = \frac{\int \eta \Pi d\eta}{\int \xi \Pi d\xi}. \quad (45)$$

The left-hand side of each of Eqs. (43)-(45) depends only on  $t$ , while their right-hand sides depend not only on  $t$ , but also  $r$  and  $z$  (as parameterized through  $\xi$  and  $\eta$ ). As such, one possible means of satisfying Eqs. (43)-(45) is to enforce

$$-\frac{R_r^{1-2\gamma} R_z^{1-\gamma}}{\ddot{R}_r} = \kappa_1 = \frac{1}{\beta} \int \xi \Pi d\xi, \quad (46)$$

$$-\frac{R_r^{2-2\gamma} R_z^{-\gamma}}{\ddot{R}_z} = \kappa_2 = \frac{1}{\beta} \int \eta \Pi d\eta, \quad (47)$$

$$\frac{R_r \ddot{R}_r}{R_z \ddot{R}_z} = \kappa_3 = \frac{\int \eta \Pi d\eta}{\int \xi \Pi d\xi}, \quad (48)$$

where the  $\kappa_i$  ( $i \in 1, 2, 3$ ) are constants. Substituting Eqs. (46) and (47) into Eq. (48), we immediately find that the each  $\kappa_i$  must satisfy the constraint

$$\kappa_3 = \frac{\kappa_2}{\kappa_1}. \quad (49)$$

First analyzing the right-hand equalities appearing in Eqs. (46)-(48), trivial rearrangements reveal various properties the otherwise arbitrary functions  $\Pi$  and  $\beta$  must feature:

$$\kappa_1 \beta = \int \xi \Pi d\xi, \quad (50)$$

$$\kappa_2 \beta = \int \eta \Pi d\eta, \quad (51)$$

$$\kappa_3 \int \xi \Pi d\xi = \int \eta \Pi d\eta, \quad (52)$$

or, differentiating Eq. (52) with respect to both  $\xi$  and  $\eta$  gives

$$\kappa_3 \xi \frac{\partial \Pi}{\partial \eta} = \eta \frac{\partial \Pi}{\partial \xi}, \quad (53)$$

which may be solved for the function  $\Pi$  appearing in Eq. (35) for the density  $\rho$  using the method of characteristics to yield

$$\Pi(\xi, \eta) = \Pi\left(\frac{\zeta^2}{2}\right), \quad (54)$$

such that  $\Pi$  is revealed to be an arbitrary function only of the generalized coordinate  $\zeta$  defined by

$$\zeta^2 \equiv \kappa_3 \xi^2 + \eta^2. \quad (55)$$

With Eq. (54), Eq. (35) then becomes

$$\rho(r, z, t) = \frac{1}{R_r^2 R_z} \Pi(\zeta). \quad (56)$$

Moreover, with Eqs. (54) and (55), the integrals appearing in Eqs. (38) and (39) for the pressure  $P$  become

$$\int \xi \Pi d\xi = \frac{\Gamma(\zeta)}{\kappa_3}, \quad (57)$$

$$\int \eta \Pi d\eta = \Gamma(\zeta), \quad (58)$$

where

$$\Gamma(\zeta) \equiv \int \zeta \Pi d\zeta, \quad (59)$$

such that both of Eqs. (57) and (58) are guaranteed to give equivalent results in light of Eq. (52); that is, Eqs. (38) and (39) become

$$\begin{aligned} P(r, z, t) &= -\frac{\ddot{R}_r}{\kappa_3 R_r R_z} \Gamma(\zeta), \\ &= -\frac{\ddot{R}_z}{R_r^2} \Gamma(\zeta). \end{aligned} \quad (60)$$

which are equivalent with Eq. (48) taken into consideration.

In addition, with Eqs. (20), (56), and (60), the SIE associated with the axisymmetric Nemchinov-Dyson solution is given by,

$$\begin{aligned} I(r, z, t) &= -\frac{R_r \ddot{R}_r}{\kappa_3 (\gamma - 1)} \Upsilon(\zeta) \\ &= -\frac{R_z \ddot{R}_z}{(\gamma - 1)} \Upsilon(\zeta), \end{aligned} \quad (61)$$

where

$$\Upsilon(\zeta) \equiv \frac{\int \zeta \Pi d\zeta}{\Pi}, \quad (62)$$

such that both representations of Eq. (61) are again guaranteed to give equivalent results in light of Eq. (48). Likewise, and also with Eqs. (26), (35), and (60), the entropy associated with the axisymmetric Nemchinov-Dyson solution is given by

$$\begin{aligned} S(r, z, t) &= -\frac{\ddot{R}_r R_r^{2\gamma-1} R_z^{\gamma-1}}{\kappa_3} \Sigma(\zeta) \\ &= -\ddot{R}_z R_r^{2\gamma-2} R_z^\gamma \Sigma(\zeta), \end{aligned} \quad (63)$$

where

$$\Sigma(\zeta) \equiv \Pi^{-\gamma} \int \zeta \Pi d\zeta, \quad (64)$$

such that both representations of Eq. (63) are again guaranteed to give equivalent results in light of Eq. (48).

Finally, turning to the left-hand equalities appearing in Eqs. (46)-(48). With Eqs. (48) and (49), Eqs. (46) and (47) are revealed to be redundant. As such,

$$-\frac{R_r^{1-2\gamma} R_z^{1-\gamma}}{\ddot{R}_r} = \kappa_1, \quad (65)$$

$$-\frac{R_r \ddot{R}_r}{R_z \ddot{R}_z} = \kappa_3, \quad (66)$$

represent the two salient coupled, second-order, nonlinear ordinary differential equations (ODEs) in the scale radii  $R_r$  and  $R_z$ ; a solution of these ODEs thus resolves the time-dependence appearing in Eqs. (56), (60), (61), and (63).

The Nemchinov-Dyson solution of Eqs. (15)-(17) and (27) is thus comprised of the  $r$  and  $z$  velocity components  $u_r$  and  $u_z$ , density  $\rho$ , pressure  $P$ , SIE  $I$ , and entropy  $S$  relations given by Eqs. (28), (29), (56), (60), (61), and (63), respectively. Each of these flow variables features two principal components:

1. Time-dependence parameterized exclusively by the scale radii  $R_r$  and  $R_z$ : these functions must satisfy the coupled, second-order, nonlinear ODE system given by Eqs. (65) and (66). Some representative solutions of these ODEs are provided in Sec. III A.
2. Spatial dependence parameterized exclusively by the function  $\Pi$ : in turn,  $\Pi$  is a function only of

the generalized coordinate  $\zeta$ , which is itself defined in terms of the dimensionless  $\xi$  and  $\eta$  variables (and hence  $r$  and  $z$ ) via Eqs. (33), (34), and (55). Otherwise, the function  $\Pi$  (and the related functions  $\beta$ ,  $\Gamma$ ,  $\Upsilon$ , and  $\Sigma$ )<sup>2</sup> is arbitrary. Some representative choices of  $\Pi$  (and their attendant physical motivations) are provided in Sec. III B.

### A. Solution Sets for $R_r$ and $R_z$

To attempt solutions of Eqs. (65) and (66), we first use Eq. (49) to write Eq. (66) as

$$\frac{R_r \ddot{R}_r}{R_z \ddot{R}_z} = \frac{\kappa_2}{\kappa_1}. \quad (67)$$

Solution of Eqs. (65) and (67) requires the introduction of four initial conditions. Without loss of generality, these initial conditions may be expressed at  $t = 0$  as

$$R_r(t=0) = R_{r,0}, \quad (68)$$

$$R_z(t=0) = R_{z,0}, \quad (69)$$

$$\dot{R}_r(t=0) = \dot{R}_{r,0}, \quad (70)$$

$$\dot{R}_z(t=0) = \dot{R}_{z,0}, \quad (71)$$

where the constants  $R_{r,0} > 0$  and  $R_{z,0} > 0$ , and the constants  $\dot{R}_{r,0}$  and  $\dot{R}_{z,0}$  are otherwise unconstrained (i.e., each may be positive, negative, or zero). In addition, Eqs. (68)-(71) further suggest that the free constants  $\kappa_1$  and  $\kappa_2$  appearing in Eqs. (65) and (67), respectively, may be written as, by evaluating Eqs. (65) and (67) themselves at  $t = 0$ ,

$$\kappa_1 = -\frac{R_{r,0}^{1-2\gamma} R_{z,0}^{1-\gamma}}{\ddot{R}_{r,0}}, \quad (72)$$

$$\kappa_2 = -\frac{R_{r,0}^{2-2\gamma} R_{z,0}^{-\gamma}}{\ddot{R}_{z,0}}, \quad (73)$$

respectively, where  $\ddot{R}_{r,0}$  and  $\ddot{R}_{z,0}$  are the second derivatives of  $R_r$  and  $R_z$  evaluated at  $t = 0$ ; as with the first derivatives these constants are unconstrained aside from being non-zero (in the interest of discarding any trivial solutions of Eqs. (65) and (67)). As such, Eqs. (72) and (73) reveal that constants  $\kappa_1$  and  $\kappa_2$  appearing in Eqs. (65) and (67), respectively, are inversely proportional to the negatives of the  $r$  and  $z$  components of an acceleration field at  $t = 0$ , respectively.

Equations (65) and (67), subject to the initial conditions given by Eqs. (68)-(71), have no known closed-form solution for arbitrary  $\gamma$ ,  $R_{r,0}$ ,  $R_{z,0}$ ,  $\dot{R}_{r,0}$ ,  $\dot{R}_{z,0}$ ,  $\ddot{R}_{r,0}$ , and  $\ddot{R}_{z,0}$ . However, various numerical solutions of this

<sup>2</sup> Though the arbitrary function  $\beta$  is related to  $\Pi$ , it is no longer needed in this study due to its relation to  $\Gamma$  via Eqs. (46)-(48).

same equation set may be broadly categorized according to their qualitative behavior in  $R_r$  and  $R_z$ , in turn resulting from different combinations of the parameters  $\dot{R}_{r,0}$ ,  $\dot{R}_{z,0}$ ,  $\ddot{R}_{r,0}$ , and  $\ddot{R}_{z,0}$ .

As tabulated in Appendix B, the salient initial parameter set including  $\dot{R}_{r,0}$ ,  $\dot{R}_{z,0}$ ,  $\ddot{R}_{r,0}$ , and  $\ddot{R}_{z,0}$  features 36 possible generic combinations, therein referred to as “cases.” These cases are generated by the following possible parameterizations, considered combinatorically:

- $\dot{R}_{r,0}$ : positive, negative, or zero,
- $\dot{R}_{z,0}$ : positive, negative, or zero,
- $\ddot{R}_{r,0}$ : positive or negative,
- $\ddot{R}_{z,0}$ : positive or negative.

Also as tabulated in Appendix B, these 36 cases allow for two distinct solution behaviors for each  $R_q$  ( $q \in r, z$ ):

1.  $R_q \rightarrow \infty$  as  $t \rightarrow -\infty$  and as  $t \rightarrow \infty$ . Globally concave-up solutions of this type are referred to as “double-regular (DR),” and manifest whenever  $\ddot{R}_{q,0} > 0$ .
2.  $R_q \rightarrow 0$  as  $t \rightarrow -t^*$  and as  $t \rightarrow t^*$ , for some  $t^* > 0$ . Globally concave-down solutions of this type are referred to as “double-singular (DS),” and manifest whenever  $\ddot{R}_{q,0} < 0$ .

The sign or value of each  $\dot{R}_{q,0}$  affects only the slope of the associated  $R_q$  curve at  $t = 0$ ; that is, these parameters only shift the otherwise symmetric  $R_q$  curves to the left or right along the  $t$ -axis, and do not otherwise materially influence the qualitative global solution behavior.

In any event, as both double regular and double singular behaviors are available for both  $R_r$  and  $R_z$ , the solutions of Eqs. (65) and (67) manifest a total of three distinct behavioral archetypes (ignoring distinctions between DR-DS and DS-DR, for example). Examples of scenarios giving rise to these three behaviors are summarized in Table I), and are discussed further in Secs. III A 1-III A 3.

Solution Type	Initial Conditions					
	$R_{r,0}$	$R_{z,0}$	$\dot{R}_{r,0}$	$\dot{R}_{z,0}$	$\ddot{R}_{r,0}$	$\ddot{R}_{z,0}$
DR-DR	1	1	1	-1/4	1	1
DS-DS	1	1	0	1	-1	-1
DR-DS	1	1	-2	0	1	-1

TABLE I: Example scenarios that give rise to the three solution archetypes arising from numerical solution of Eqs. (65) and (67), subject to the initial conditions given by Eqs. (68)-(71).

### 1. DR-DR Solutions

An example of an initial data parameterization that gives rise to a DR-DR type solution (i.e., both  $R_r$  and  $R_z$

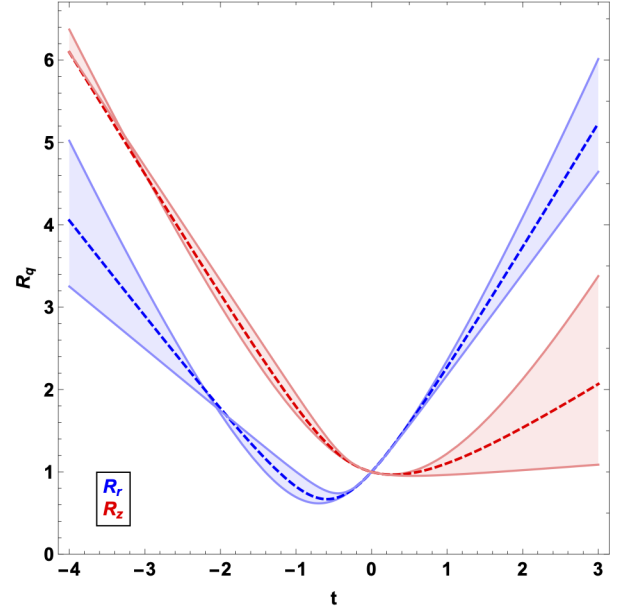


FIG. 3 DR-DR solution of Eqs. (65) and (67), with Eqs. (68)-(71) set to the values appearing in the first row of Table I. Shaded regions indicate a range of  $\gamma$  parameterizations including  $\gamma \in [1.1, 3.0]$ ; in each case the dashed line corresponds to  $\gamma = 5/3$ .

are double-regular, or globally concave-up) of Eqs. (65) and (67) with Eqs. (68)-(71) is given in the first row of Table I, so that with Eqs. (72), (73), and (49),  $\kappa_1 = -1$ ,  $\kappa_2 = -1$ , and  $\kappa_3 = 1$ . The numerical solution of Eqs. (65) and (67) with Eqs. (68)-(71) under the aforementioned parameterization is depicted in Fig. 3, for several choices of the adiabatic index  $\gamma$ .

From the physical standpoint, the DR-DR behavior exemplified in Fig. 3 manifests whenever  $\ddot{R}_{r,0} > 0$  and  $\ddot{R}_{z,0} > 0$ , indicating that the global acceleration field is entirely positive at  $t = 0$ , and remains so for all  $t$ . Consequently, both  $R_r$  and  $R_z$  are observed to diverge as  $|t| \rightarrow \infty$ .

Otherwise, Fig. 3 also features the trend that for sufficiently large  $|t|$ , both  $R_r$  and  $R_z$  increase with decreasing adiabatic index  $\gamma$ . In turn, for given initial conditions, this trend demonstrates that  $R_r$  and  $R_z$  evolve more rapidly in early or late time as  $\gamma \rightarrow 1$ . This trend is physically plausible in that the ideal gas compressibility increases with decreasing  $\gamma$ ; in this sense, the “small  $\gamma$ ” systems are expected to be more dynamically responsive (i.e., less rigid).

### 2. DS-DS Solutions

An example of an initial data parameterization that gives rise to a DS-DS type solution (i.e., both  $R_r$  and  $R_z$  are double-singular, or globally concave-down) of Eqs. (65) and (67) with Eqs. (68)-(71) is given by the



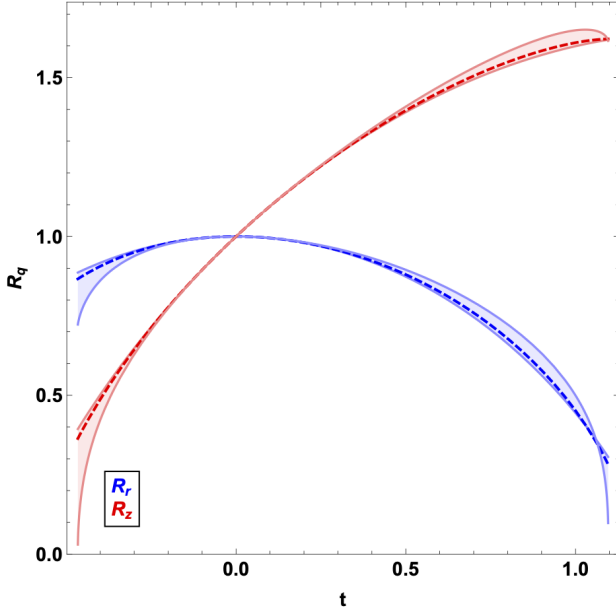


FIG. 4 DS-DS solution of Eqs. (65) and (67), with Eqs. (68)-(71) set to the values appearing in the middle row of Table I. Shaded regions indicate a range of  $\gamma$  parameterizations including  $\gamma \in [1.1, 3.0]$ ; in each case the dashed line corresponds to  $\gamma = 5/3$ .

second row of Table I, so that with Eqs. (72), (73), and (49),  $\kappa_1 = 1$ ,  $\kappa_2 = 1$ , and  $\kappa_3 = 1$ . The numerical solution of Eqs. (65) and (67) with Eqs. (68)-(71) under the aforementioned parameterization is depicted in Fig. 4, for several choices of the adiabatic index  $\gamma$ .

From the physical standpoint, the DS-DS behavior exemplified in Fig. 4 manifests whenever  $\ddot{R}_{r,0} < 0$  and  $\ddot{R}_{z,0} < 0$ , indicating that the global acceleration field is entirely negative at  $t = 0$ , and remains so for all  $t$ . Consequently, both  $R_r$  and  $R_z$  are observed to converge as  $|t| > 0$ . For the specific examples depicted in Fig. 4, in each featured case one of  $R_r$  or  $R_z$  reaches zero “first” (i.e., at some  $t = |t^*|$  smaller than the corresponding  $t = |t^*|$  associated with the other  $R_q$ ), after which the overall solution ceases to have physical meaning.

Otherwise, Fig. 4 also features the same trends with respect to the adiabatic index  $\gamma$  as observed and explained in Sec. III A 1. The value of  $t = |t^*|$  at which the solution terminates depends strongly on  $\gamma$ .

### 3. DR-DS Solutions

An example of an initial data parameterization that gives rise to a DR-DS type solution (i.e., one each of  $R_r$  and  $R_z$  is double-regular or globally concave-up and double-singular or globally concave-down) of Eqs. (65) and (67) with Eqs. (68)-(71) is given by the final row of Table I so that with Eqs. (72), (73), and (49),  $\kappa_1 = -1$ ,  $\kappa_2 = 1$ , and  $\kappa_3 = -1$ . The numerical solution of Eqs. (65)

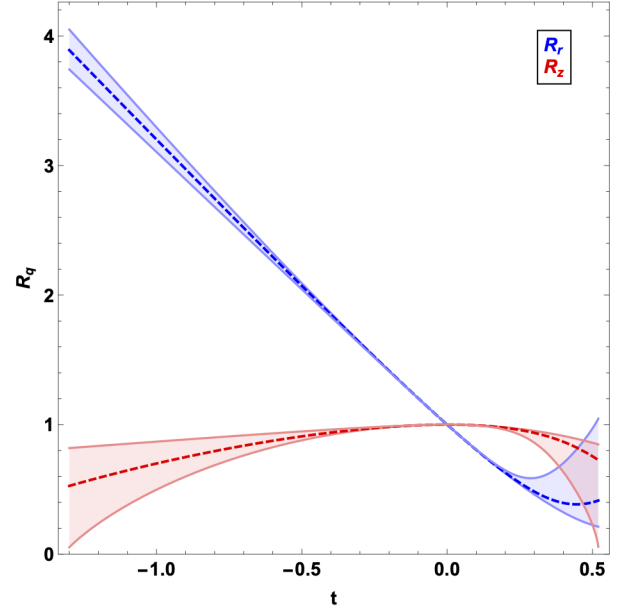


FIG. 5 DR-DS solution of Eqs. (65) and (67), with Eqs. (68)-(71) set to the values appearing in the final row of Table I. Shaded regions indicate a range of  $\gamma$  parameterizations including  $\gamma \in [1.1, 3.0]$ ; in each case the dashed line corresponds to  $\gamma = 5/3$ .

and (67) with Eqs. (68)-(71) under the aforementioned parameterization is depicted in Fig. 5, for several choices of the adiabatic index  $\gamma$ .

From the physical standpoint, the DR-DS behavior exemplified in Fig. 5 manifests whenever  $\ddot{R}_{r,0} > 0$  and  $\ddot{R}_{z,0} < 0$  (or vice versa), indicating that the global acceleration field is positive in one direction and negative in the other at  $t = 0$ , and remains so for all  $t$ . Consequently, one of  $R_r$  and  $R_z$  is observed to diverge as  $|t| > 0$ , while the other is observed to converge. For the specific examples depicted in Fig. 5, in each featured case only  $R_z$  reaches zero at two times, after which the overall solution ceases to have physical meaning.

Otherwise, Fig. 5 also features the same trends with respect to the adiabatic index  $\gamma$  as observed and explained in Secs. III A 1 and III A 2.

## B. Solution Sets for II

As noted by Sedov [1] in the context of the 1D linear velocity solutions, in the axisymmetric Nemchinov-Dyson solution given by Eqs. (28), (29), (56), (60), (61), and (63), the arbitrary functions  $\Pi$ ,  $\Gamma$ ,  $\Upsilon$ , and  $\Sigma$  are

“...directly related to the entropy distribution through the gas.”

This notion is of course explicitly true by definition [i.e., in light of Eq. (63)] for the function  $\Sigma$ , and in due course

$\Pi$ ,  $\Gamma$ , and  $\Upsilon$  according to Eqs. (59), (62), and (64). However, aside from Eq. (54), no additional constraints are available in the underlying formulation of the ideal gas inviscid Euler equations for the resolution of the otherwise arbitrary functional forms in  $\zeta$  of  $\Pi$ ,  $\Gamma$ ,  $\Upsilon$ , and  $\Sigma$ .

Indeed, this degree of arbitrariness appearing in the axisymmetric Nemchinov-Dyson solution (or, more broadly, any solution of the ideal gas inviscid Euler equations featuring linear velocity assumptions) is a direct result of the lack of dissipation mechanisms (e.g., viscosity or heat conduction) appearing in Eqs. (1)-(3). On the other hand, the inclusion of any such mechanism in Eqs. (1)-(3) provides an additional constraint that must be satisfied in addition to Eq. (54), and so selects unique (but self-consistent) forms of  $\Pi$ ,  $\Gamma$ ,  $\Upsilon$ , and  $\Sigma$ . An example of this phenomenology is provided by Hendon and Ramsey [56], in the context of 1D linear velocity solutions featuring a thermal radiation diffusion process in an ideal gas.

This outcome is expected due to the classically established thermodynamical connections between dissipation and entropy generation. In particular, according to the Second Law of Thermodynamics, a dissipative or irreversible process not only transforms energy from one form to another, but also produces entropy at a specified rate. In the context of fluid flow scenarios, the prescribed functional form of a dissipative process sets this rate, and thus constrains the entropy  $S$  (or the function  $\Sigma$ , and so  $\Pi$ ,  $\Gamma$ , and  $\Upsilon$ ). In the absence of such a mechanism - such as in Eqs. (1)-(3) - no dissipation rate is available to be calculated and thus further constrain the underlying thermodynamics, and  $\Pi$ ,  $\Gamma$ ,  $\Upsilon$ , and  $\Sigma$  therefore remain arbitrary unless another ancillary constraint is provided.

In this case, the functional form of  $\Pi$  in  $\zeta$  [and through their definitions given by Eqs. (59), (62), and (64),  $\Gamma$ ,  $\Upsilon$ , and  $\Sigma$ ] appearing in the axisymmetric Nemchinov-Dyson solution therefore remains arbitrary, and thus may be prescribed according to target flow patterns of interest. Four such examples are provided in Secs. III B 1-III B 4, and are depicted in Fig. 6.

### 1. Uniform Density Solutions

The form of the function  $\Pi$  associated with a uniform (i.e., constant in spatial coordinates, but not necessarily in time) density distribution is given by

$$\Pi(\zeta) = \Pi_0, \quad (74)$$

where the otherwise arbitrary constant  $\Pi_0 > 0$  so that the density given by Eq. (56) is positive definite and thus physically realistic. With Eq. (74), the related functions  $\Gamma$ ,  $\Upsilon$ , and  $\Sigma$  defined by Eqs. (59), (62), and (64), respec-

tively, realize as

$$\Gamma(\zeta) = \frac{\Pi_0 \zeta^2}{2} + \Gamma_0, \quad (75)$$

$$\Upsilon(\zeta) = \frac{\zeta^2}{2} + \frac{\Gamma_0}{\Pi_0}, \quad (76)$$

$$\Sigma(\zeta) = \frac{\Pi_0^{1-\gamma} \zeta}{2} + \Pi_0^{-\gamma} \Gamma_0, \quad (77)$$

where  $\Gamma_0$  is an arbitrary integration constant, the sign of which must be selected so that the pressure, SIE, and entropy given by Eqs. (60), (61), and (63) are positive definite and thus physically realistic. The pressure and SIE distributions associated with a uniform density distribution are thus revealed to be parabolic in  $\zeta$ , while the entropy distribution is revealed to be linear in  $\zeta$ .

Equations (74)-(77) are depicted in Fig. 6 for the example parameterization  $\gamma = 5/3$ ,  $\Pi_0 = 1$ , and  $\Gamma_0 = 0$ .

### 2. Uniform SIE Solutions

The form of the function  $\Upsilon$  associated with a uniform (i.e., constant in  $r$  and  $z$ , but not necessarily in  $t$ ) SIE (or temperature) distribution is given by

$$\Upsilon(\zeta) = \Upsilon_0, \quad (78)$$

where  $\Upsilon_0$  is an arbitrary constant, the sign of which must be selected so that the SIE given by Eq. (61) is positive definite and thus physically realistic. With Eqs. (62) and (76), the related function  $\Pi$  then satisfies

$$\Upsilon_0 = \frac{\int \zeta \Pi d\zeta}{\Pi}, \quad (79)$$

or, equivalently, after differentiating Eq. (79) with respect to  $\zeta$ ,

$$\Upsilon_0 \frac{d\Pi}{d\zeta} - \zeta \Pi = 0, \quad (80)$$

the solution of which is given by

$$\Pi(\zeta) = \Pi_0 \exp\left(\frac{\zeta^2}{2\Upsilon_0}\right), \quad (81)$$

where the otherwise arbitrary integration constant  $\Pi_0 > 0$  so that the density given by Eq. (56) is positive definite and thus physically realistic. With Eq. (81), the related functions  $\Gamma$  and  $\Sigma$  defined by Eqs. (59) and (64), respectively, realize as

$$\Gamma(\zeta) = \Pi_0 \Upsilon_0 \exp\left(\frac{\zeta^2}{2\Upsilon_0}\right), \quad (82)$$

$$\Sigma(\zeta) = \Pi_0^{1-\gamma} \Upsilon_0 \exp\left[\frac{(1-\gamma)\zeta^2}{2\Upsilon_0}\right]. \quad (83)$$

The density, pressure, and entropy distributions associated with a uniform SIE distribution are thus revealed to be Gaussian in  $\zeta$ .

Equations (78), (81), (82), and (83) are depicted in Fig. 6 for the example parameterization  $\gamma = 5/3$ ,  $\Pi_0 = 1$ , and  $\Upsilon_0 = -1$ .

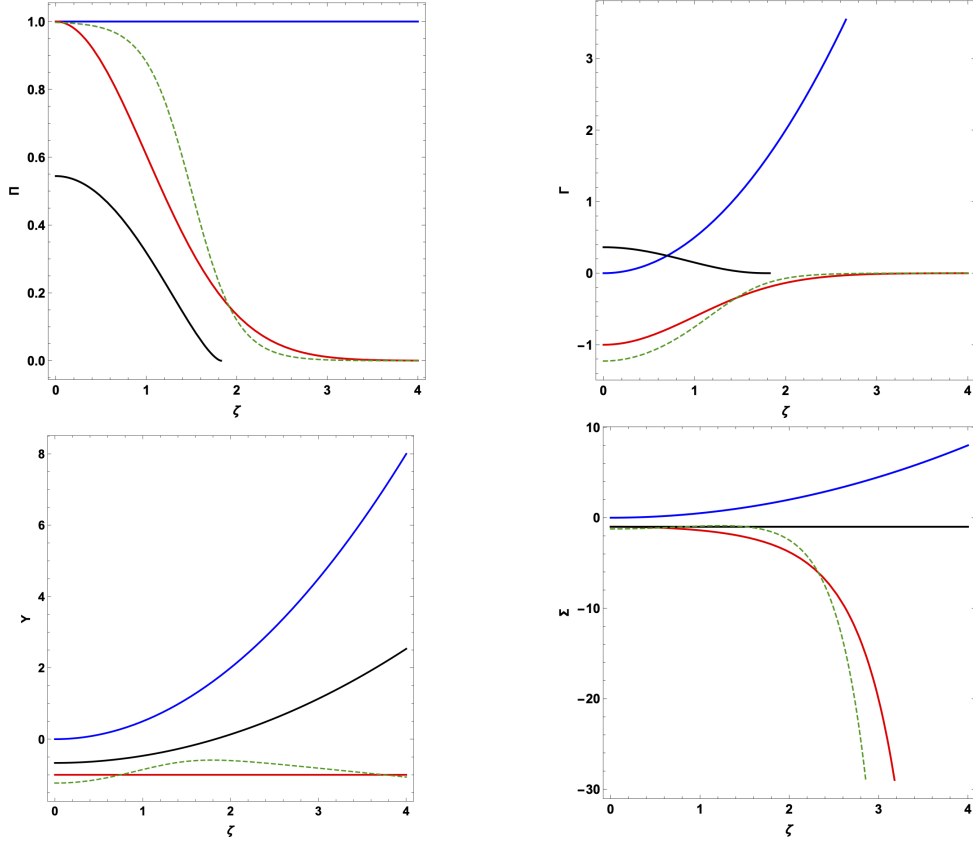


FIG. 6 The functions  $\Pi(\zeta)$  (top left),  $\Gamma(\zeta)$  (top right),  $\Upsilon(\zeta)$  (bottom left), and  $\Sigma(\zeta)$  (bottom right) for the uniform density (solid blue), uniform SIE (solid red), uniform entropy (solid black), and diffuse surface (dashed green) solutions.

### 3. Uniform Entropy Solutions

The form of the function  $\Sigma$  associated with a uniform (i.e., constant in  $r$  and  $z$ , but not necessarily in  $t$ ) entropy distribution is given by

$$\Sigma(\zeta) = \Sigma_0, \quad (84)$$

where  $\Sigma_0$  is an arbitrary constant, the sign of which must be selected so that the entropy given by Eq. (63) is positive definite and thus physically realistic. With Eqs. (64) and (84), the related function  $\Pi$  then satisfies

$$\Sigma_0 = -\Pi^{-\gamma} \int \zeta \Pi d\zeta, \quad (85)$$

or, equivalently, after differentiating Eq. (85) with respect to  $\zeta$ ,

$$\gamma \Sigma_0 \Pi^{\gamma-1} \frac{d\Pi}{d\zeta} + \zeta \Pi = 0, \quad (86)$$

the solution of which is given by

$$\Pi(\zeta) = \left[ (\gamma - 1) \Pi_0 + \frac{(\gamma - 1) \zeta^2}{2\gamma \Sigma_0} \right]^{\frac{1}{\gamma-1}}, \quad (87)$$

where  $\Pi_0$  is an arbitrary integration constant. With Eq. (81), the related functions  $\Gamma$  and  $\Upsilon$  defined by Eqs. (59) and (62), respectively, realize as

$$\Gamma(\zeta) = -\Pi_0 S_0 \left[ (\gamma - 1) \Pi_0 + \frac{(\gamma - 1) \zeta^2}{2\gamma \Sigma_0} \right]^{\frac{\gamma}{\gamma-1}}, \quad (88)$$

$$\Upsilon(\zeta) = \frac{(\gamma - 1) (2\gamma \Pi_0 \Sigma_0 + \zeta^2)}{2\gamma}, \quad (89)$$

indicating the sign of the otherwise arbitrary constant  $\Pi_0$  must be selected in conjunction with that of  $\Sigma_0$  so that the pressure given by Eq. (60) is positive definite and thus physically realistic. The density and pressure distributions associated with a uniform entropy distribution are thus revealed to follow power laws in  $\zeta$ , while the SIE distribution is revealed to be quadratic in  $\zeta$ .

Equations (84), (87), (88), and (89) are depicted in Fig. 6 for the example parameterization  $\gamma = 5/3$ ,  $\Pi_0 = 1$ , and  $\Sigma_0 = -1$ .

### 4. Diffuse Surface Solutions

For an otherwise arbitrary constant  $\Pi_0 > 0$ , so that the density given by Eq. (56) is positive definite and thus

physically realistic, a form of the function  $\Pi$  given by

$$\Pi(\zeta) = \frac{\Pi_0}{1 + \exp\left(\frac{\zeta}{\zeta_0} - \zeta_1\right)}, \quad (90)$$

corresponds to a distribution approximately satisfying

$$\Pi(\zeta) \approx \begin{cases} \Pi_0 & \zeta \leq \zeta^* \\ 0 & \zeta \geq \zeta^* \end{cases}, \quad (91)$$

where the parameter  $\zeta^*$  is defined in terms of the constants  $\zeta_0 > 0$  and  $\zeta_1 > 0$  by

$$\zeta^* \equiv \zeta_0 \zeta_1, \quad (92)$$

that is,  $\zeta^*$  represents the point where  $\Pi = \frac{\Pi_0}{2}$ . This “boundary” between the “non-zero” and “zero” portions Eq. (90) is in fact continuous, but becomes increasingly sharp or less “diffuse” as  $\zeta_1 \rightarrow \infty$ . As such, axisymmetric Nemchinov-Dyson solutions featuring Eq. (90) are referred to as “diffuse surface” solutions.

With Eq. (90), the related functions  $\Gamma$ ,  $\Upsilon$ , and  $\Sigma$  defined by Eqs. (59), (62), and (64), respectively, realize as

$$\Gamma(\zeta) = \zeta_0 \Pi_0 \left[ \zeta \ln \left( \frac{1}{1 + \exp\left(\frac{\zeta}{\zeta_0} - \zeta_1\right)} \right) + \zeta_0 \text{Li}_2 \left( -\exp \left( \zeta_1 - \frac{\zeta}{\zeta_0} \right) \right) \right] + \Gamma_0, \quad (93)$$

$$\begin{aligned} \Upsilon(\zeta) = & \zeta_0 \left[ 1 + \exp \left( \frac{\zeta}{\zeta_0} - \zeta_1 \right) \right] \\ & \times \left[ \zeta \ln \left( \frac{1}{1 + \exp \left( \zeta_1 - \frac{\zeta}{\zeta_0} \right)} \right) + \zeta_0 \text{Li}_2 \left( -\exp \left( \zeta_1 - \frac{\zeta}{\zeta_0} \right) \right) \right] \\ & + \frac{1 + \exp \left( \frac{\zeta}{\zeta_0} - \zeta_1 \right)}{\Pi_0} \Gamma_0, \end{aligned} \quad (94)$$

$$\begin{aligned} \Sigma(\zeta) = & \zeta_0 \Pi_0^{1-\gamma} \left[ 1 + \exp \left( \frac{\zeta}{\zeta_0} - \zeta_1 \right) \right]^\gamma \\ & \times \left[ \zeta \ln \left( \frac{1}{1 + \exp \left( \zeta_1 - \frac{\zeta}{\zeta_0} \right)} \right) + \zeta_0 \text{Li}_2 \left( -\exp \left( \zeta_1 - \frac{\zeta}{\zeta_0} \right) \right) \right] \\ & + \frac{\left[ 1 + \exp \left( \frac{\zeta}{\zeta_0} - \zeta_1 \right) \right]^\gamma}{\Pi^\gamma} \Gamma_0, \end{aligned} \quad (95)$$

where  $\Gamma_0$  is an arbitrary integration constant, the sign of which must be selected so that the pressure, SIE, and entropy given by Eqs. (60), (61), and (63) are positive

definite and thus physically realistic, and  $\text{Li}_2$  is the second order Jonquière’s (polylogarithm) function<sup>3</sup>. The pressure, SIE, and entropy distributions associated with a diffuse surface density distribution are thus revealed to be highly non-trivial in  $\zeta$ .

Equations (90)-(95) are depicted in Fig. 6 for the example parameterization including

$$\Gamma_0 = -\Pi_0 \zeta_0^2 \text{Li}_2 [-\exp(\zeta_1)], \quad (96)$$

so that  $\Gamma(\zeta = 0) = 0$ , and  $\gamma = 5/3$ ,  $\Pi_0 = 1$ ,  $\zeta_0 = 1/4$ , and  $\zeta_1 = 6$ .

#### IV. EXAMPLE AXISYMMETRIC NEMCHINOV-DYSON SOLUTIONS

The various elements appearing in Secs. III A and III B (and their many alternate parameterizations) may be combined into Eqs. (28), (29), (56), (60), (61), and (63) to yield a limitless number of axisymmetric Nemchinov-Dyson solutions of Eqs. (15)-(17) and (27). A common feature among these possible solutions is their manifestation as a collection of axisymmetric conic sections of revolution whose eccentricities vary with time.

More precisely, and inclusive of figures of infinite spatial extent, in light of Eq. (55) axisymmetric Nemchinov-Dyson solutions include density, pressure, SIE, and entropy solution fields featuring ellipsoidal, circular, or hyperbolic constant-value contours; the eccentricity of each of these “level surfaces” varies with time. In particular, if each of Eqs. (56), (60), (61), and (63) is generically written as

$$\varphi(r, z, t) = \tau(t) \Psi(\zeta^2), \quad (97)$$

for a non-constant but otherwise invertible function  $\Psi$  (i.e., with inverse function  $\Psi^{-1}$ ), the time-dependent level surface associated with the constant state variable  $\varphi = \varphi_0$  is defined by

$$\zeta^2 = \Psi^{-1} \left[ \frac{\varphi_0}{\tau(t)} \right], \quad (98)$$

or, with Eq. 55,

$$\frac{\kappa_3 r^2}{a_r^2} + \frac{z^2}{a_z^2} = 1, \quad (99)$$

where  $a_r^2(t)$  and  $a_z^2(t)$  are defined by

$$a_r^2 \equiv R_r^2 \Psi^{-1} \left[ \frac{\varphi_0}{\tau(t)} \right], \quad (100)$$

$$a_z^2 \equiv R_z^2 \Psi^{-1} \left[ \frac{\varphi_0}{\tau(t)} \right]. \quad (101)$$

<sup>3</sup> An alternate form can be written as the complete Fermi-Dirac integral. Indeed, we find that  $\text{Li}_2(-e^x) = -\frac{1}{\Gamma(2)} \int_0^\infty \frac{t}{e^{t-x} + 1} dt$  where the gamma function is  $\Gamma(2) = 1$  and  $x = 4\zeta - 6$ .

Depending on the sign of the constant  $\kappa_3$ , Eq. (99) defines either an ellipse ( $\kappa_3 > 0$ ) or a hyperbola ( $\kappa_3 < 0$ ) in  $(r, z)$ -space, the eccentricity of which varies according to the behavior in time of both  $a_r$  and  $a_z$ . In particular, for  $\kappa_3 > 0$ , the eccentricity of any ellipsoidal level surfaces is given by

$$e = \sqrt{1 - \min\left(\frac{a_r^2}{a_z^2}, \frac{a_z^2}{a_r^2}\right)}, \quad (102)$$

or, with Eqs. (100) and (101),

$$e = \sqrt{1 - \min\left(\frac{R_r^2}{R_z^2}, \frac{R_z^2}{R_r^2}\right)}, \quad (103)$$

which is independent of both the level surface value  $\varphi_0$  and the functional form  $\Psi$  of the solution field; as such, the eccentricity of all ellipsoidal level surfaces in all state variables for a given Nemchinov-Dyson solution depends only on the scale radii  $R_r(t)$  and  $R_z(t)$ .

Similarly, for  $\kappa_3 < 0$ , the eccentricity of any hyperbolic level surfaces is given by

$$e = \sqrt{1 + \frac{a_r^2}{a_z^2}}, \quad (104)$$

or, with Eqs. (100) and (101),

$$e = \sqrt{1 + \frac{R_r^2}{R_z^2}}, \quad (105)$$

which is again independent of both the level surface value  $\phi_0$  and the functional form  $\Psi$  of the solution field; as such, the eccentricity of all hyperbolic level surfaces in all state variables for a given Nemchinov-Dyson solution again depends only on the scale radii  $R_r(t)$  and  $R_z(t)$ .

Under this construction, three example axisymmetric Nemchinov-Dyson solutions are given in Secs. IV A-IV C.

#### A. Uniform SIE DR-DR Solution

As a first example, a “uniform SIE DR-DR” axisymmetric Nemchinov-Dyson solution follows from combining the results appearing in Secs. III A 1 and III B 2. This solution is given by Eqs. (28) and (29) for  $u_r(r, z, t)$  and  $u_z(r, z, t)$ , respectively, and, with Eqs. (33), (34), (55),

(56), (60), (61), (63), (78), (81), (82), and (83),

$$\begin{aligned} \rho(r, z, t) &= \frac{\Pi_0}{R_r^2 R_z} \left[ (\gamma - 1) \Pi_0 + \frac{(\gamma - 1) \zeta^2}{2\gamma \Sigma_0} \right]^{\frac{1}{\gamma-1}} \\ &\quad \times \exp\left(\frac{\kappa_3 r^2}{2\Upsilon_0 R_r^2} + \frac{z^2}{2\Upsilon_0 R_z^2}\right), \end{aligned} \quad (106)$$

$$P(r, z, t) = -\Pi_0 \Upsilon_0 \frac{R_r \ddot{R}_r}{\kappa_3 R_r^2 R_z} \exp\left(\frac{\kappa_3 r^2}{2\Upsilon_0 R_r^2} + \frac{z^2}{2\Upsilon_0 R_z^2}\right), \quad (107)$$

$$I(r, z, t) = -\frac{R_r \ddot{R}_r}{\kappa_3 (\gamma - 1)} \Upsilon_0, \quad (108)$$

$$\begin{aligned} S(r, z, t) &= -\Pi_0^{1-\gamma} \Upsilon_0 \frac{\ddot{R}_r R_r^{2\gamma-1} R_z^{\gamma-1}}{\kappa_3} \exp\left[\frac{(1-\gamma) \kappa_3 r^2}{2\Upsilon_0 R_r^2} \right. \\ &\quad \left. + \frac{(1-\gamma) z^2}{2\Upsilon_0 R_z^2}\right], \end{aligned} \quad (109)$$

where  $\Pi_0 > 0$  and  $\Upsilon_0 < 0$  are otherwise arbitrary constants. For the DR-DR type solution provided in Sec. III A 1,  $\kappa_3 = 1$  as appearing in Eqs. (106)-(109), and the numerical representations of  $R_r$  and  $R_z$  are depicted in Fig. 3.

Equations (28), (29), (106), (107), and (109) are depicted in Figs. 7 and 8, for the example parameterization  $\Pi_0 = 1$ ,  $\Upsilon_0 = -1$ , and  $\gamma = 5/3$ , and featuring the  $\gamma = 5/3$  DR-DR numerical solution depicted in Fig. 3. The associated time-dependent eccentricity of all ellipsoidal level surfaces in the density, pressure, and entropy state variables is given by Eq. (103), and is provided in Fig. 6. Finally, the associated Eq. (108) is independent of both  $r$  and  $z$  by construction (i.e., it assumes the same time-dependent value at every spatial point within the solution field); therefore only its time-dependence is depicted in Fig. 10.

Figure 7 depicts the total velocity vector field associated with the DR-DR type solution [as Eqs. (28) and (29) hold whether the spatial portion of the associated Nemchinov-Dyson solution is of uniform SIE type or not] featured in Sec. III A 1, including the appropriate, conjoined linear behavior in both  $r$  and  $z$ . The directions of the various velocity vectors appearing in Fig. 7 are directly proportional to the slopes of the  $R_r$  and  $R_z$  curves appearing in Fig. 3, as otherwise explicitly revealed by Eqs. (28) and (29). That is, whenever  $\dot{R}_r > 0$  or  $\dot{R}_z > 0$  in Fig. 4, the associated velocity vector is pointed “outward” in the appropriate direction in Fig. 7, and whenever  $\dot{R}_r < 0$  or  $\dot{R}_z < 0$  in Fig. 4, the associated velocity vector is pointed “inward” in the appropriate direction in Fig. 7. For the DR-DR example depicted in Figs. 3 and 7, the global motion of the associated uniform SIE solution is therefore largely dominated by motion in  $r$  for all times.

Figure 8 indicates that all density, pressure, and entropy level surfaces are indeed ellipsoidal in shape, and (as depicted) continuously deform from prolate to oblate with increasing time, while also rarefying and depressurizing. Furthermore, Fig. 9 shows that these level surfaces

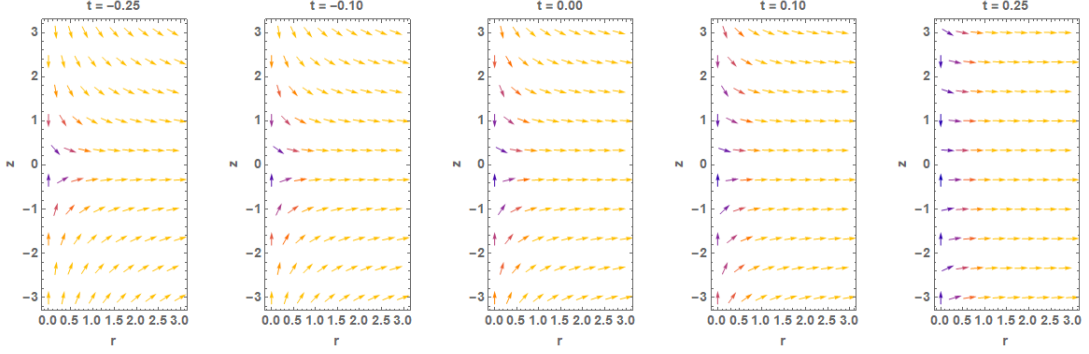


FIG. 7 Equations (28) and (29) evaluated at various times, featuring the  $\gamma = 5/3$  DR-DR numerical solution depicted in Fig. 3.

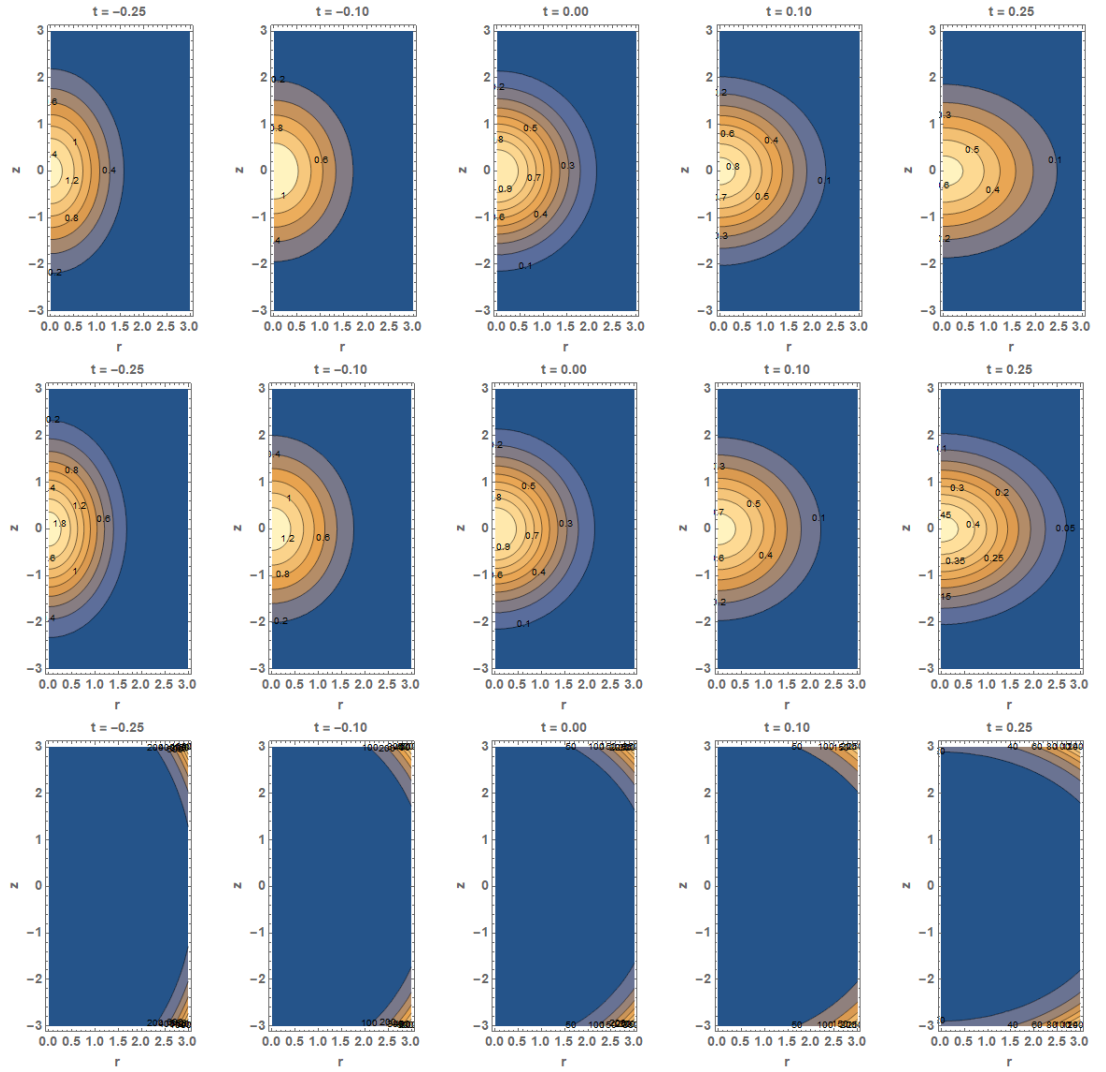


FIG. 8 Equations (106), (107), and (109) (top, middle, and bottom rows, respectively) evaluated at various times, under the example parameterization  $\Pi_0 = 1$ ,  $\Upsilon_0 = -1$ , and  $\gamma = 5/3$ , and featuring the  $\gamma = 5/3$ ,  $\kappa_3 = 1$  DR-DR numerical solution depicted in Fig. 3.

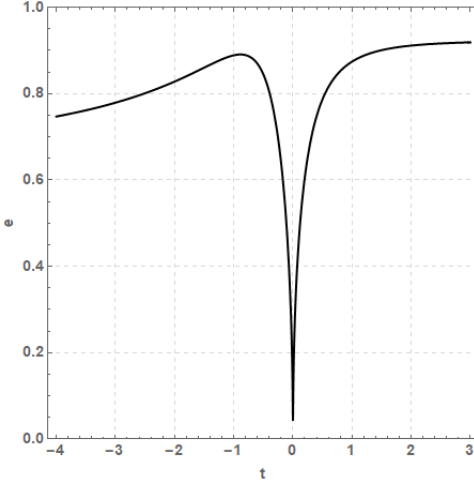


FIG. 9 Equation (103) evaluated at various times, featuring the  $\gamma = 5/3$ ,  $\kappa_3 = 1$  DR-DR numerical solution depicted in Fig. 3.

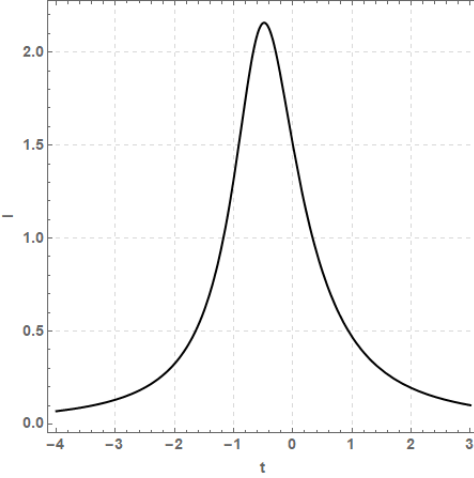


FIG. 10 Equation (108) evaluated at various times, under the example parameterization  $\Pi_0 = 1$ ,  $\Upsilon_0 = -1$ , and  $\gamma = 5/3$ , and featuring the  $\gamma = 5/3$ ,  $\kappa_3 = 1$  DR-DR numerical solution depicted in Fig. 3.

vary rapidly between high eccentricity ( $e > 0.8$ ) and perfect sphericity ( $e = 0.0$ ) in the neighborhood of  $t = 0$  [by design, in light of Eqs. (68) and (69)]. Otherwise, the  $r$  and  $z$  variation of the density, pressure, and entropy solutions proceeds according to variously sharp Gaussian distributions, as also indicated by Eqs. (106), (107), and (109).

Finally, Fig. 10 shows that the spatially constant SIE increases rapidly from small to peak values near  $t = 0$ , and afterward again decreasing rapidly. The maximum SIE occurs shortly before  $t = 0$ , thus corresponding to an event other than the solution field attaining perfect spherical symmetry. Rather, on the grounds of physical intuition, the SIE is maximized whenever the specific kinetic energy of the solution field is simultaneously min-

imized, which may be verified by inspection of Fig. 3. From Fig. 3 and Eqs. (28) and (29), the specific kinetic energy of the Nemchinov-Dyson solution is proportional to the square of the slopes of the  $R_r$  and  $R_z$  curves. Therefore, the time at which these slopes (i.e.,  $\dot{R}_r$  and  $\dot{R}_z$ ) are jointly minimized is the same time at which the maximum SIE is observed to occur in Fig. 10.

## B. Uniform Entropy DS-DS Solution

As a second example, a “uniform entropy DS-DS” axisymmetric Nemchinov-Dyson solution follows from combining the results appearing in Secs. III A 2 and III B 3. This solution is again given by Eqs. (28) and (29) for  $u_r(r, z, t)$  and  $u_z(r, z, t)$ , respectively, and, with Eqs. (33), (34), (55), (56), (60), (61), (63), (84), (87), (88), and (89),

$$\rho(r, z, t) = \frac{1}{R_r^2 R_z} \left[ (\gamma - 1) \Pi_0 + \frac{\gamma - 1}{2\gamma \Sigma_0} \left( \frac{\kappa_3 r^2}{R_r^2} + \frac{z^2}{R_z^2} \right) \right]^{\frac{1}{\gamma-1}}, \quad (110)$$

$$P(r, z, t) = \frac{\Pi_0 \Sigma_0 R_r \ddot{R}_r}{\kappa_3 R_r^2 R_z} \left[ (\gamma - 1) \Pi_0 + \frac{\gamma - 1}{2\gamma \Sigma_0} \left( \frac{\kappa_3 r^2}{R_r^2} + \frac{z^2}{R_z^2} \right) \right]^{\frac{\gamma}{\gamma-1}}, \quad (111)$$

$$I(r, z, t) = -\frac{R_r \ddot{R}_r}{2\gamma \kappa_3} \left[ 2\gamma \Pi_0 \Sigma_0 \left( \frac{\kappa_3 r^2}{R_r^2} + \frac{z^2}{R_z^2} \right) \right], \quad (112)$$

$$S(r, z, t) = -\frac{\Sigma_0 \ddot{R}_r R_r^{2\gamma-1} R_z^{\gamma-1}}{\kappa_3}, \quad (113)$$

where  $\Pi_0 < 0$  and  $\Sigma_0 > 0$  are arbitrary constants. For the DS-DS type solution provided in Sec. III A 2,  $\kappa_3 = 1$  as appearing in Eqs. (110)-(113), and the numerical representations of  $R_r$  and  $R_z$  are depicted in Fig. 4.

Equations (28), (29), (110), (111), and (112) are depicted in Figs. 11 and 12, for the example parameterization  $\Pi_0 = -1$ ,  $\Sigma_0 = 1$ , and  $\gamma = 5/3$ , and featuring the  $\gamma = 5/3$  DS-DS numerical solution depicted in Fig. 4. The associated time-dependent eccentricity of all ellipsoidal level surfaces in the density, pressure, and SIE state variables is given by Eq. (103), and is provided in Fig. 6. Finally, the associated Eq. (113) is independent of both  $r$  and  $z$  by construction (i.e., it assumes the same time-dependent value at every spatial point within the solution field); therefore only its time-dependence is depicted in Fig. 14.

Figure 11 depicts the total velocity vector field associated with the DS-DS type solution [as Eqs. (28) and (29) hold whether the spatial portion of the associated Nemchinov-Dyson solution is of uniform entropy type or not] featured in Sec. III A 2, including the appropriate, conjoined linear behavior in both  $r$  and  $z$ . The directions of the various velocity vectors appearing in Fig. 11 are again directly proportional to the slopes of the  $R_r$  and

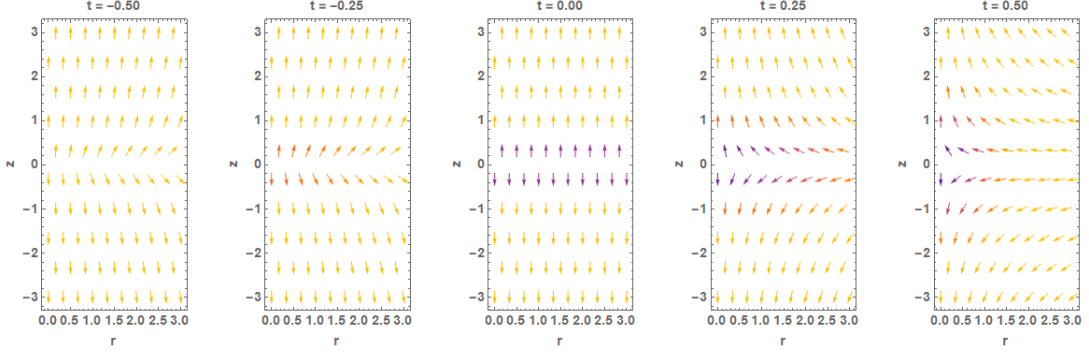


FIG. 11 Equations (28) and (29) evaluated at various times, featuring the  $\gamma = 5/3$  DS-DS numerical solution depicted in Fig. 4.

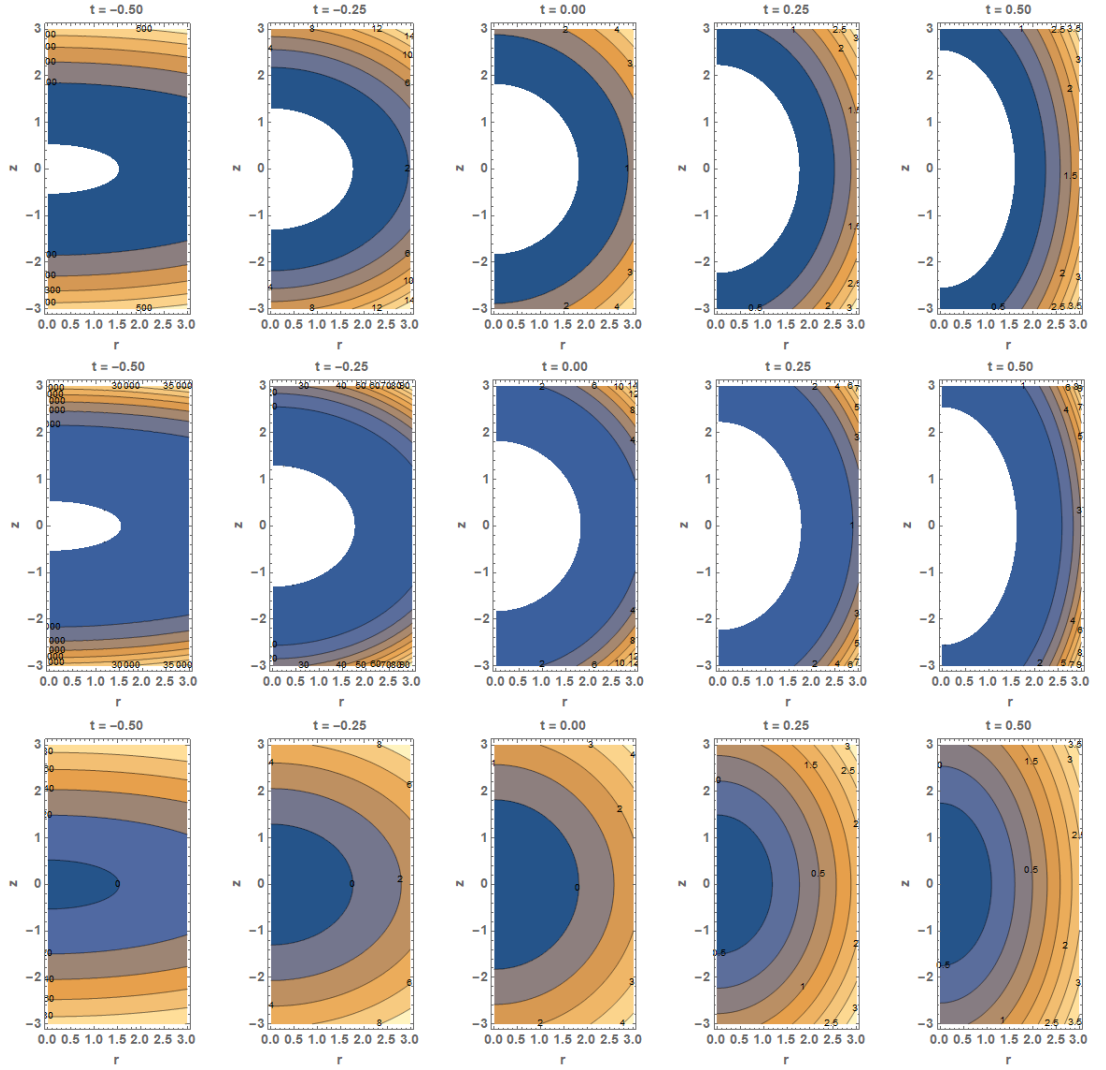


FIG. 12 Equations (110), (111), and (112) (top, middle, and bottom rows, respectively) evaluated at various times, under the example parameterization  $\Pi_0 = -1$ ,  $\Sigma_0 = -1$ , and  $\gamma = 5/3$ , and featuring the  $\gamma = 5/3$ ,  $\kappa_3 = 1$  DS-DS numerical solution depicted in Fig. 4.



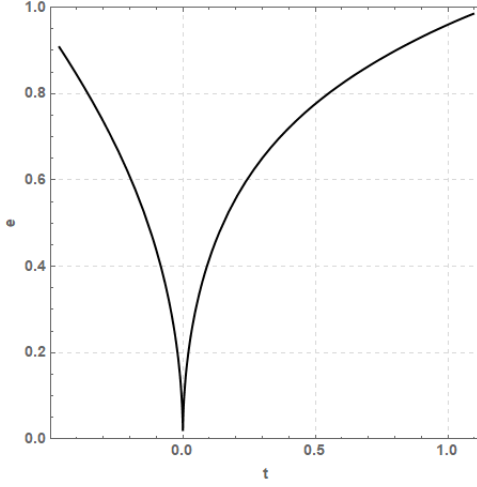


FIG. 13 Equation (103) evaluated at various times, featuring the  $\gamma = 5/3$ ,  $\kappa_3 = 1$  DS-DS numerical solution depicted in Fig. 4.

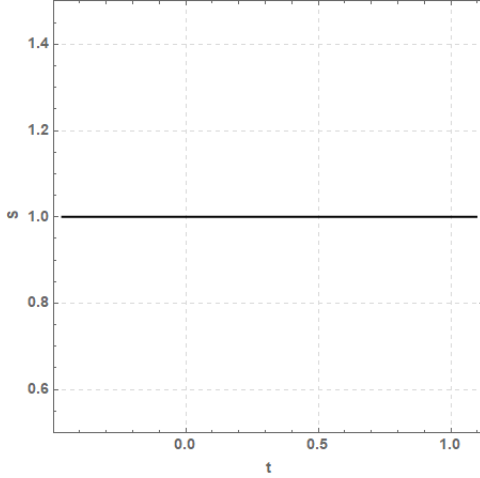


FIG. 14 Equation (109) evaluated at various times, under the example parameterization  $\Pi_0 = -1$ ,  $\Sigma_0 = 1$ , and  $\gamma = 5/3$ , and featuring the  $\gamma = 5/3$ ,  $\kappa_3 = 1$  DS-DS numerical solution depicted in Fig. 4.

$R_z$  curves appearing in Fig. 4, as otherwise explicitly revealed by Eqs. (28) and (29). For the DS-DS example depicted in Figs. 4 and 11, the global motion of the associated uniform entropy solution is therefore largely dominated by motion in  $z$  for  $t \leq 0$ , and becomes increasingly dominated by motion in  $r$  at later times.

Figure 12 depicts the presence of an ellipsoidal “cavity” in the solution field surrounding  $r = z = 0$ ; the density and pressure given by Eqs. (110) and (111) are not real-valued in that region, though the SIE and entropy given by Eqs. (112) and (113) are defined there. Figure 12 further indicates that all density, pressure, and SIE level surfaces exterior to the cavity surface are indeed ellipsoidal in shape, and (as depicted) continuously deform from oblate to prolate with increasing time, while also rarefy-

ing, depressurizing, and cooling. Furthermore, Fig. 13 shows that these level surfaces vary rapidly between extremely high eccentricity ( $e > 0.9$ ) to perfect sphericity ( $e = 0.0$ ) in the neighborhood of  $t = 0$  [by design, in light of Eqs. (68) and (69)]. Otherwise, the  $r$  and  $z$  variation of the density, pressure, and SIE solutions proceeds according to variously sharp power-law distributions, as also indicated by Eqs. (110), (111), and (112).

Finally, Fig. 14 shows that the spatially constant entropy is also constant in time, indicating that the solution is purely homentropic.

### C. Diffuse Surface DR-DS Solution

As a final example, a “diffuse surface DR-DS” axisymmetric Nemchinov-Dyson solution follows from combining the results appearing in Secs. III A 3 and III B 4. This solution is again given by Eqs. (28) and (29) for  $u_r(r, z, t)$  and  $u_z(r, z, t)$ , respectively, and, with Eqs. (33), (34), (55), (56), (60), (61), (63), (90), (93), (94), and (95),

$$\rho(r, z, t) = \frac{\Pi_0}{R_r^2 R_z} \frac{1}{1 + \exp\left(\sqrt{\frac{\kappa_3 r^2}{\zeta_0^2 R_r^2} + \frac{z^2}{\zeta_0^2 R_z^2}} - \zeta_1\right)}, \quad (114)$$

$$\begin{aligned} P(r, z, t) = & -\frac{R_r \ddot{R}_r}{\kappa_3 R_r^2 R_z} \\ & \times \left\{ \frac{\Pi_0}{4} \zeta_0 \ln \left( \frac{1}{1 + \exp\left(\sqrt{\frac{\kappa_3 r^2}{\zeta_0^2 R_r^2} + \frac{z^2}{\zeta_0^2 R_z^2}} - \zeta_1\right)} \right) \right. \\ & - \frac{\Pi_0}{16} \text{Li}_2 \left[ -\exp \left( \zeta_1 - \sqrt{\frac{\kappa_3 r^2}{\zeta_0^2 R_r^2} + \frac{z^2}{\zeta_0^2 R_z^2}} \right) \right] \\ & \left. + -\frac{R_r \ddot{R}_r}{\kappa_3 R_r^2 R_z} \Gamma_0 \right\}, \quad (115) \end{aligned}$$

$$\begin{aligned} I(r, z, t) = & \frac{R_r \ddot{R}_r}{\kappa_3 (\gamma - 1)} \left\{ \zeta_0 \left[ 1 + \exp \left( \sqrt{\frac{\kappa_3 r^2}{\zeta_0^2 R_r^2} + \frac{z^2}{\zeta_0^2 R_z^2}} - \zeta_1 \right) \right] \right. \\ & \times \left[ \zeta \ln \left( \frac{1}{1 + \exp \left( \sqrt{\frac{\kappa_3 r^2}{\zeta_0^2 R_r^2} + \frac{z^2}{\zeta_0^2 R_z^2}} - \zeta_1 \right)} \right) \right] \\ & + \zeta_0 \text{Li}_2 \left( -\exp \left( \zeta_1 - \sqrt{\frac{\kappa_3 r^2}{\zeta_0^2 R_r^2} + \frac{z^2}{\zeta_0^2 R_z^2}} \right) \right) \left. \right] \\ & + \frac{1 + \exp \left( \sqrt{\frac{\kappa_3 r^2}{\zeta_0^2 R_r^2} + \frac{z^2}{\zeta_0^2 R_z^2}} - \zeta_1 \right)}{\Pi_0} \Gamma_0 \left. \right\}, \quad (116) \end{aligned}$$

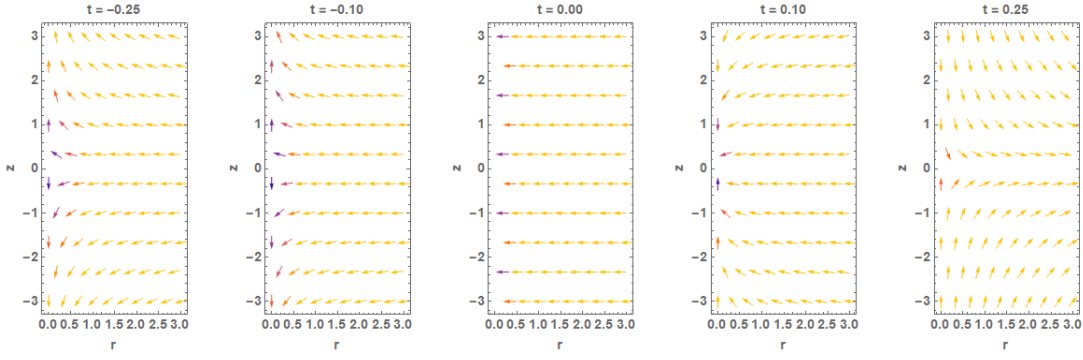


FIG. 15 Equations (28) and (29) evaluated at various times, featuring the  $\gamma = 5/3$  DR-DS numerical solution depicted in Fig. 5.

$$\begin{aligned}
 S(r, z, t) = & -\frac{\ddot{R}_r R_r^{2\gamma-1} R_z^{\gamma-1}}{\kappa_3} \zeta_0 \Pi_0^{1-\gamma} \\
 & \times \left\{ \left[ 1 + \exp \left( \sqrt{\frac{\kappa_3 r^2}{\zeta_0^2 R_r^2} + \frac{z^2}{\zeta_0^2 R_z^2}} - \zeta_1 \right) \right]^\gamma \right. \\
 & \times \left[ \zeta \ln \left( \frac{1}{1 + \exp \left( \sqrt{\frac{\kappa_3 r^2}{\zeta_0^2 R_r^2} + \frac{z^2}{\zeta_0^2 R_z^2}} - \zeta_1 \right)} \right) \right. \\
 & \left. \left. + \zeta_0 \text{Li}_2 \left( -\exp \left( \zeta_1 - \sqrt{\frac{\kappa_3 r^2}{\zeta_0^2 R_r^2} + \frac{z^2}{\zeta_0^2 R_z^2}} \right) \right) \right] \right. \\
 & \left. + \frac{\left[ 1 + \exp \left( \sqrt{\frac{\kappa_3 r^2}{\zeta_0^2 R_r^2} + \frac{z^2}{\zeta_0^2 R_z^2}} - \zeta_1 \right) \right]^\gamma}{\Pi^\gamma} \Gamma_0 \right\} \\
 & , \tag{117}
 \end{aligned}$$

where  $\Pi_0 > 0$ ,  $\Gamma_0$ ,  $\zeta_0 > 0$ , and  $\zeta_1 > 0$  are otherwise arbitrary constants. For the DR-DS type solution provided in Sec. III A 3,  $\kappa_3 = -1$  as appearing in Eqs. (114)-(117), and the numerical representations of  $R_r$  and  $R_z$  are depicted in Fig. 5.

Equations (28), (29), and (114)-(117) are depicted in Figs. 15 and 16, for the example parameterization  $\Pi_0 = 1$ ,  $\Gamma_0$  given by Eq. (96),  $\zeta_0 = 1/4$ ,  $\zeta_1 = 6$ , and  $\gamma = 5/3$ , and featuring the  $\gamma = 5/3$  DR-DS numerical solution depicted in Fig. 5. The associated time-dependent eccentricity of all hyperbolic level surfaces in the density, pressure, SIE, and entropy state variables is given by Eq. (105), and is provided in Fig. 6.

Figure 15 depicts the total velocity vector field associated with the DR-DS type solution [as Eqs. (28) and (29) hold whether the spatial portion of the associated Nemchinov-Dyson solution is of diffuse surface type or not] featured in Sec. III A 3, including the appropriate, conjoined linear behavior in both  $r$  and  $z$ . The directions of the various velocity vectors appearing in Fig. 15 are again directly proportional to the slopes of the  $R_r$  and  $R_z$  curves appearing in Fig. 5, as otherwise explicitly revealed by Eqs. (28) and (29). For the DR-DS example depicted in Figs. 5 and 15, the global motion of

the associated diffuse surface solution is therefore largely dominated for most times by motion in  $r$ , and exhibits a sign reversal at later times.

Figure 16 indicates the presence of a double-conical “outer surface” in the diffuse surface DR-DS solution field; all state variables are not real-valued beyond that surface. Moreover, Fig. 16 indicates that with increasing time the outer surface “opens up,” while the material within simultaneously compresses, pressurizes, and heats. Figure 16 also shows that all hyperbolic state variable level surfaces diminish in eccentricity with increasing time. Otherwise, the  $r$  and  $z$  variation of the density, pressure, SIE, and entropy solutions proceeds according to highly non-trivial distributions, as also indicated by Eqs. (114)-(117).

## V. DISCUSSION AND CONCLUSION

In the spirit of and similar to the wealth of analogous results appearing within the existing literature, the results of Sec. III define a general procedure for the construction of an infinite variety of Nemchinov-Dyson solutions of the 2D axisymmetric inviscid Euler equations, coupled to an ideal gas EOS. The solutions derived using this recipe share several common features, including:

- Space-time separability in each component of the velocity field. Moreover, this separable form is constrained to be linear in each associated direction, thus yielding a class of uniformly expanding or contracting solutions.
- Self-consistent but otherwise arbitrary state variable distributions that depend solely on a 2D elliptical or hyperbolic spatial coordinate. That the functional forms of these state variables in this coordinate are arbitrary owes to the lack of dissipation mechanisms within the attendant formulation of the inviscid Euler equations.
- The non-trivial level surfaces for all state variables (when they exist) are either elliptical or hyperbolic

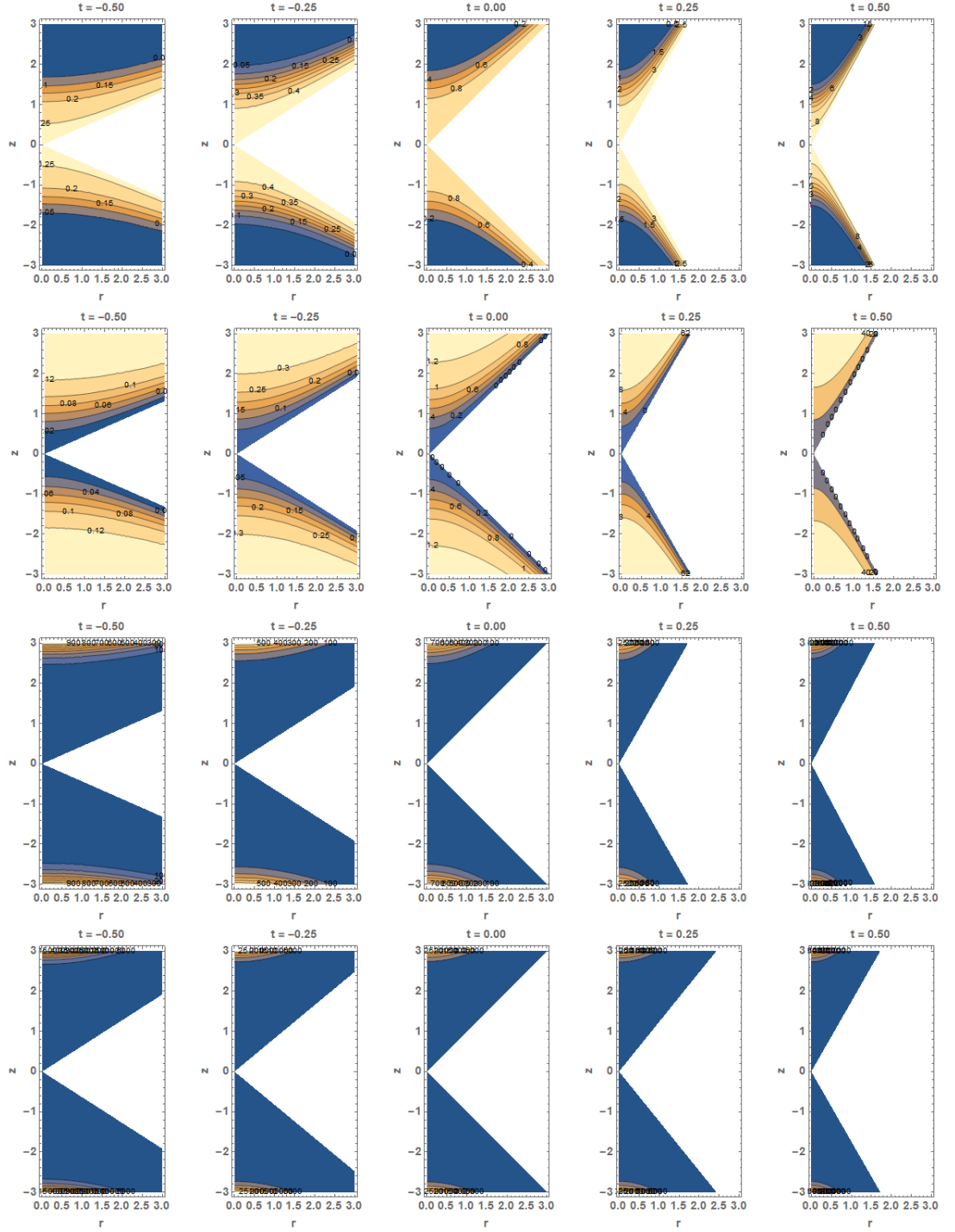


FIG. 16 Equations (114), (115), (116), and (117) (first through fourth rows, respectively) evaluated at various times, under the example parameterization  $\Pi_0 = 1$ ,  $\Gamma_0$  given by Eq. (96),  $\zeta_0 = 1/4$ ,  $\zeta_1 = 6$ , and  $\gamma = 5/3$ , and featuring the  $\gamma = 5/3$ ,  $\kappa_3 = -1$  DR-DS numerical solution depicted in Fig. 5.

surfaces in  $(r, z)$  space, and otherwise form surfaces of revolution about the 2D axisymmetric  $z$ -axis. Both the character and dynamical behavior of these level surfaces is associated with the sign of the solution's conjoined acceleration field (i.e., whether the acceleration field is positive or negative in each

direction for all times).

Three example axisymmetric Nemchinov-Dyson solutions are provided in Secs. IV A-IV C. The uniform SIE DR-DR solution appearing in Sec. IV A may be regarded as a “classical” solution in that it features ellipsoidal state

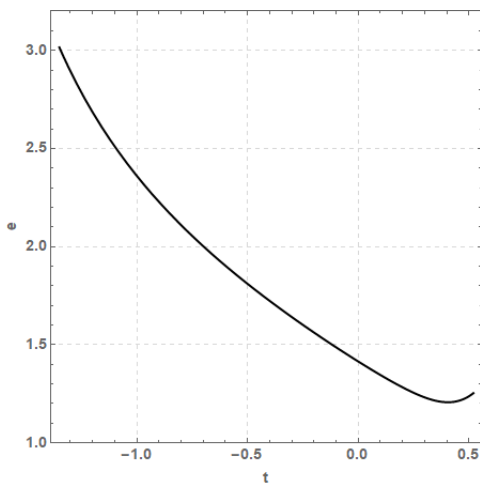


FIG. 17 Equation (105) evaluated at various times, featuring the  $\gamma = 5/3$ ,  $\kappa_3 = -1$  DR-DS numerical solution depicted in Fig. 5.

variable level surfaces that first contract and then expand in both the  $r$  and  $z$  directions. The uniform entropy DS-DS solution appearing in Sec. IV B is in a sense the “inverse” of similar DR-DR solutions as disseminated by Nemchinov [27], in that instead of featuring a discrete object that either expands or contracts, it features a distending ellipsoidal cavity embedded within an otherwise infinite expanse of fluid. The diffuse surface DR-DS solution appearing in Sec. IV C is entirely new and separate from the others, in that it features a distending, infinite double-cone figure with hyperbolic level surfaces in all interior state variables.

Without a doubt, analogous (and possibly other) solution behaviors are also extractable from the more extensive existing models featuring 3D Cartesian geometries. Even so, the absence from the existing literature of some of the more exotic solutions derived herein is likely due to historical, application-driven realities: conical or hyperbolic linear velocity solutions, for example, appear to have little relevance to practical scenarios rooted in astrophysics or elsewhere. On the other hand, the expanding and contracting cavity solutions derived in this work (or implicitly contained in this work’s broader result set) may have some utility in the fields of bubble collapse or cavitation, as otherwise discussed by Boyd et al [57].

Finally, and as discussed in Sec. I, any of the solutions derived as part of this program of study are expected to be of direct use in quantitative code verification or model qualification studies associated with inviscid Euler codes designed for the numerical solution of, for example, Eqs. (1)-(3). In this sense, some of the more exotic solutions presented as part of Sec. IV - or their near neighbors - may find broader use beyond their limited physical implications, should they eventually come to serve as especially challenging or otherwise unique test problems or model solutions.

## A. Recommendations for Future Study

From a purely theoretical standpoint, the results of Sec. III B will no doubt prove readily extensible to a limitless variety of potential counterparts. A few examples of concrete physical significance (and with pedigree as established within the voluminous literature on solutions of the inviscid Euler equations featuring linear velocity assumptions) are provided in Secs. III B 1-III B 4, but others arising from analogous application-based motivations may of course be devised and coupled to any of the dynamical behaviors examined in Sec. III A. This potential program of study represents perhaps the most straightforward path for further extension of the results appearing in Secs. III B 1-III B 4.

With additional relevance to Sec. III A, and inspired by the work of Gaffet, the dynamical system given by Eqs. (65) and (67) may in a special case or cases prove amenable to analytical solution, or at the very least expression in terms of quadratures or special functions (e.g., elliptic integrals). A more detailed analytical study of Eqs. (65) and (67) thus appears to be in order, perhaps using the same techniques as rooted in conservation law or symmetry analysis theories, and as previously employed in the context of the inviscid Euler equations by Gaffet or Coggeshall [15–17]. If they exist, any analytical or even semi-analytical solutions obtained through such means will prove invaluable for a more comprehensive understanding of the physical and mathematical properties of any affiliated axisymmetric Nemchinov-Dyson solutions.

More broadly, the symmetry analysis formalism that may be brought to bear on Eqs. (65) and (67) may also be used to better categorize and understand the physical implications of the axisymmetric Nemchinov-Dyson solutions themselves. For example, McHardy et al. [46] recently applied this technique in the context of linear velocity solutions of the 1D inviscid Euler equations, and discovered that not all such solutions necessarily share (or, more appropriately, are generated by) the same underlying symmetry properties. In addition to potentially yielding similar benefits in the context of axisymmetric Nemchinov-Dyson solutions, the symmetry analysis formalism also represents the best way to explicitly connect the results of this and related work to that of, for example, Coggeshall [15–17].

Otherwise, numerous modeling generalizations of this work are also available, including but not limited to:

- Use of non-ideal alternatives to Eq. (20), such as the stiffened gas or Mie-Grüneisen EOS forms as disseminated by Harlow and Amsden [47], or various other forms depending on a practical application of interest),
- Coupling of Eqs. (1)-(3) to various additional physical mechanisms (some of which are dissipative) such as gravitation, viscosity, heat transport, charge transport, and/or electromagnetism.

- Investigation of Eqs. (1)-(3) as written in other 2D and 3D geometries.
- Incorporation of rotational motion into the underlying mathematical framework, in the style of many existing solutions as disseminated by, for example, Ovsianikov [25, 26], Dyson [30], and their many successors.

In conjunction with the linear velocity assumption as formulated within a given coordinate system, all of these generalizations may be combined in various ways to yield an ever-growing family of Nemchinov-Dyson solutions of increasing physical fidelity or application relevance.

Beyond even these non-trivial generalizations, further expansion of this work may be affected by either somehow enhancing or dispensing with the linear velocity assumption itself. Perhaps the lowest order generalization along these lines involves retaining space-time separability in each velocity field component (regardless of the underlying geometry), and subsequently investigating various non-uniform spatial velocity profiles. Several examples of non-linear velocity profiles also appear in, for example, the work of Coggeshall [15–17].

In addition to this potentially extensive program of purely theoretical study, the rigorous exercise of 2D or 3D Nemchinov-Dyson solutions for the purposes of quantitative code verification or model qualification also remains as relatively unbroken ground. As noted in Sec. I, some quantitative code verification studies along these lines have been performed in the context of the 1D linear velocity solutions, but even the existing 2D and 3D solutions featuring the same underlying assumptions appear to have been much less utilized in this manner. Naturally, perhaps the most practical future use of the many results derived in this work (and the body of existing work upon which our results are founded) will be in the quantitative code verification context, or for use as diagnostic tools for computational simulations of more complicated physical processes. Indeed, and in closing, as appropriately noted by Sachdev [58],

“...understanding the validity and place of exact/approximate analytical solution[s] in the general context can be greatly enhanced by numerical simulation. In short, there must be a continuous interplay of analysis and computation if a ... problem is to be successfully tackled.”

## ACKNOWLEDGMENTS

The authors dedicate this work to the late Freeman J. Dyson, and also the late Paul P. Whalen (who introduced SDR to this interesting topic).

This work was supported by the U.S. Department of Energy (DOE) through the Los Alamos National Laboratory. Los Alamos National Laboratory is operated by Triad National Security, LLC, for the National Nuclear Security Administration of the DOE (contract number 89233218CNA000001). JFG was partially funded through supported by the National Science Foundation (NSF) under Grant No. PHY-1803912. The authors thank E. J. Albright, D. B. Garcia, P. J. Jaegers, J. D. McHardy, E. M. Schmidt, J. H. Schmidt, and B. A. Temple for their valuable insights on these topics. JFG thanks Prof. Richard F. Lebed (Arizona State University) for his insight and support.

## Appendix A: Curvilinear Euler Equations

As shown in Ref. [55], in general, the material derivative for a vector field  $\vec{A}(q_1, q_2, q_3, t)$  with fluid velocity  $\vec{v}(q_1, q_2, q_3, t)$  is

$$\sum_{j=1}^3 \left[ \left( \vec{v} \cdot \vec{\nabla} \right) \vec{A} \right]_j = \sum_{i,j=1}^3 \frac{v_i}{h_i} \frac{\partial A_j}{\partial q_i} + \frac{A_i}{h_i h_j} \left( v_j \frac{\partial h_j}{\partial q_i} - v_i \frac{\partial h_i}{\partial q_j} \right), \quad (\text{A1})$$

where  $h_i$  are the Lamé coefficients for the specific geometry. For a scalar field  $\varphi(q_1, q_2, q_3, t)$ , we find

$$\vec{v} \cdot \vec{\nabla} \varphi = \sum_{i=1}^3 \frac{v_i}{h_i} \frac{\partial \varphi}{\partial q_i}. \quad (\text{A2})$$

We can also write the divergence of  $\vec{A}(q_1, q_2, q_3, t)$  as

$$\vec{\nabla} \cdot \vec{A} = \sum_{i=1}^3 \left( \prod_{j=1}^3 h_j^{-1} \right) \frac{\partial}{\partial q_i} \left( A_i \prod_{j \neq i} h_j \right), \quad (\text{A3})$$

while the gradient of a scalar field  $\varphi(q_1, q_2, q_3, t)$

$$\vec{\nabla} \varphi = \sum_{i=1}^3 \frac{1}{h_i} \frac{\partial \varphi}{\partial q_i} \hat{e}_i, \quad (\text{A4})$$

for orthonormal unit vector  $\hat{e}_i$ .

We now substitute Eqs. (A1)-(A4) into Eqs. (1)-(3) and have

$$\begin{aligned} \frac{\partial \rho}{\partial t} + \frac{u_1}{h_1} \frac{\partial \rho}{\partial q_1} + \frac{u_2}{h_2} \frac{\partial \rho}{\partial q_2} + \frac{u_3}{h_3} \frac{\partial \rho}{\partial q_3} + \rho \left[ \frac{1}{h_1} \frac{\partial u_1}{\partial q_1} + \frac{1}{h_2} \frac{\partial u_2}{\partial q_2} + \frac{1}{h_3} \frac{\partial u_3}{\partial q_3} + u_1 \left( \frac{1}{h_1 h_3} \frac{\partial h_2}{\partial q_1} + \frac{1}{h_1 h_2} \frac{\partial h_3}{\partial q_1} \right) \right. \\ \left. + u_2 \left( \frac{1}{h_1 h_2} \frac{\partial h_3}{\partial q_2} + \frac{1}{h_2 h_3} \frac{\partial h_1}{\partial q_2} \right) + u_3 \left( \frac{1}{h_2 h_3} \frac{\partial h_1}{\partial q_3} + \frac{1}{h_1 h_3} \frac{\partial h_2}{\partial q_3} \right) \right] = 0, \quad (\text{A5}) \end{aligned}$$

$$\frac{\partial u_1}{\partial t} + \frac{u_1}{h_1} \frac{\partial u_1}{\partial q_1} + \frac{u_2}{h_2} \frac{\partial u_1}{\partial q_2} + \frac{u_3}{h_3} \frac{\partial u_1}{\partial q_3} + \frac{u_2}{h_1 h_2} \left( u_1 \frac{\partial h_1}{\partial q_2} - u_2 \frac{\partial h_2}{\partial q_1} \right) + \frac{u_3}{h_1 h_3} \left( u_1 \frac{\partial h_1}{\partial q_3} - u_3 \frac{\partial h_3}{\partial q_1} \right) + \frac{1}{\rho} \frac{1}{h_1} \frac{\partial P}{\partial q_1} = 0, \quad (\text{A6})$$

$$\frac{\partial u_2}{\partial t} + \frac{u_1}{h_1} \frac{\partial u_2}{\partial q_1} + \frac{u_2}{h_2} \frac{\partial u_2}{\partial q_2} + \frac{u_3}{h_3} \frac{\partial u_2}{\partial q_3} + \frac{u_1}{h_1 h_2} \left( u_2 \frac{\partial h_2}{\partial q_1} - u_1 \frac{\partial h_1}{\partial q_2} \right) + \frac{u_3}{h_2 h_3} \left( u_2 \frac{\partial h_2}{\partial q_3} - u_3 \frac{\partial h_3}{\partial q_2} \right) + \frac{1}{\rho} \frac{1}{h_2} \frac{\partial P}{\partial q_2} = 0, \quad (\text{A7})$$

$$\frac{\partial u_3}{\partial t} + \frac{u_1}{h_1} \frac{\partial u_3}{\partial q_1} + \frac{u_2}{h_2} \frac{\partial u_3}{\partial q_2} + \frac{u_3}{h_3} \frac{\partial u_3}{\partial q_3} + \frac{u_1}{h_1 h_3} \left( u_3 \frac{\partial h_3}{\partial q_1} - u_1 \frac{\partial h_1}{\partial q_3} \right) + \frac{u_2}{h_2 h_3} \left( u_3 \frac{\partial h_3}{\partial q_2} - u_2 \frac{\partial h_2}{\partial q_3} \right) + \frac{1}{\rho} \frac{1}{h_3} \frac{\partial P}{\partial q_3} = 0, \quad (\text{A8})$$

$$\begin{aligned} \frac{\partial E}{\partial t} + \frac{u_1}{h_1} \frac{\partial E}{\partial q_1} + \frac{u_2}{h_2} \frac{\partial E}{\partial q_2} + \frac{u_3}{h_3} \frac{\partial E}{\partial q_3} + \frac{1}{\rho} \left[ \frac{u_1}{h_1} \frac{\partial P}{\partial q_1} + \frac{u_2}{h_2} \frac{\partial P}{\partial q_2} + \frac{u_3}{h_3} \frac{\partial P}{\partial q_3} + \frac{P}{h_1} \frac{\partial u_1}{\partial q_1} + \frac{P}{h_2} \frac{\partial u_2}{\partial q_2} + \frac{P}{h_3} \frac{\partial u_3}{\partial q_3} \right. \\ \left. + P u_1 \left( \frac{1}{h_1 h_2} \frac{\partial h_2}{\partial q_1} + \frac{1}{h_1 h_3} \frac{\partial h_3}{\partial q_1} \right) + P u_2 \left( \frac{1}{h_2 h_3} \frac{\partial h_3}{\partial q_2} + \frac{1}{h_1 h_2} \frac{\partial h_1}{\partial q_2} \right) + P u_3 \left( \frac{1}{h_1 h_3} \frac{\partial h_1}{\partial q_3} + \frac{1}{h_2 h_3} \frac{\partial h_2}{\partial q_3} \right) \right] = 0. \quad (\text{A9}) \end{aligned}$$

For cylindrical coordinates,  $(q_1, q_2, q_3) \rightarrow (r, \phi, z)$  and the Lamé coefficients are  $(h_1, h_2, h_3) \rightarrow (1, r, 1)$ . The Nemchinov-Dyson problem considered in Sec. III only deals with isotropic fluid flow. Therefore, is no dependence on  $\phi$  in Eqs. (15)-(18).

## Appendix B: Cases for $R_r(t)$ and $R_z(t)$

Initial Conditions								Solution Type
$R_{r,0}$	$R_{z,0}$	$\dot{R}_{r,0}$	$\dot{R}_{z,0}$	$\ddot{R}_{r,0}$	$\ddot{R}_{z,0}$	$\kappa_1$	$\kappa_2$	
1	1	1	-1	1	1	-1	-1	DR-DR
1	1	1	1	1	1	-1	-1	DR-DR
1	1	1	0	1	1	-1	-1	DR-DR
1	1	0	0	1	1	-1	-1	DR-DR
1	1	0	1	1	1	-1	-1	DR-DR
1	1	0	-1	1	1	-1	-1	DR-DR
1	1	-1	0	1	1	-1	-1	DR-DR
1	1	-1	-1	1	1	-1	-1	DR-DR
1	1	-1	1	1	1	-1	-1	DR-DR
1	1	1	-1	-1	-1	1	1	DS-DS
1	1	1	1	-1	-1	1	1	DS-DS
1	1	1	0	-1	-1	1	1	DS-DS
1	1	0	0	-1	-1	1	1	DS-DS
1	1	0	1	-1	-1	1	1	DS-DS
1	1	0	-1	-1	-1	1	1	DS-DS
1	1	-1	0	-1	-1	1	1	DS-DS
1	1	-1	-1	-1	-1	1	1	DS-DS
1	1	-1	1	-1	-1	1	1	DS-DS
1	1	1	-1	1	-1	-1	1	DR-DS
1	1	1	1	1	-1	-1	1	DR-DS
1	1	1	0	1	-1	-1	1	DR-DS
1	1	0	0	1	-1	-1	1	DR-DS
1	1	0	1	1	-1	-1	1	DR-DS
1	1	0	-1	1	-1	-1	1	DR-DS
1	1	-1	0	1	-1	-1	1	DR-DS
1	1	-1	-1	1	-1	-1	1	DR-DS
1	1	-1	1	1	-1	-1	1	DR-DS
1	1	1	-1	-1	1	1	-1	DR-DS
1	1	1	1	-1	1	1	-1	DR-DS
1	1	1	0	-1	1	1	-1	DR-DS
1	1	0	0	-1	1	1	-1	DR-DS
1	1	0	1	-1	1	1	-1	DR-DS
1	1	0	-1	-1	1	1	-1	DR-DS
1	1	-1	0	-1	1	1	-1	DR-DS
1	1	-1	-1	-1	1	1	-1	DR-DS
1	1	-1	1	-1	1	1	-1	DR-DS

TABLE II: Shown are the 36 possible combinations for initial conditions outlined in Sec. III A. Unlike Tab. I, only positive and negative integers are tabulated.

- 
- [1] L. I. Sedov, *Similarity and dimensional methods in mechanics* (CRC press, 2018).
- [2] Y. Zel'dovich and Y. Raizer, *Physics of Shock Waves and High-Temperature Hydrodynamic Phenomena*, Dover Books on Physics (Dover Publications, 2012).
- [3] B. Cantwell, *Introduction to Symmetry Analysis*, Cambridge Texts in Applied Mathematics (Cambridge University Press, 2002).
- [4] S. Atzeni and J. Meyer-ter Vehn, *The physics of inertial fusion: beam plasma interaction, hydrodynamics, hot dense matter*, Vol. 125 (OUP Oxford, 2004).
- [5] K. P. Stanyukovich, *Unsteady motion of continuous media* (Elsevier, 2016).
- [6] P. Sachdev, *Shock waves & explosions* (CRC Press, 2016).
- [7] H. Motz, London and New York, Academic Press, 1979, 299 p. (1979).
- [8] G. J. Pert, *Journal of Fluid Mechanics* **100**, 257–277 (1980).
- [9] G. J. Pert, *Journal of Plasma Physics* **41**, 263–280 (1989).
- [10] R. Kidder, *Nuclear Fusion* **14**, 53 (1974).
- [11] R. Kidder, *Nuclear Fusion* **14**, 797 (1974).
- [12] R. Kidder, *Nuclear Fusion* **16**, 3 (1976).
- [13] H. Hora, in *Laser Interaction and Related Plasma Phenomena*, edited by H. J. Schwarz and H. Hora (Springer US, Boston, MA, 1971) pp. 365–382.
- [14] H. Hora and D. Pfirsch, in *Laser Interaction and Related Plasma Phenomena*, edited by H. J. Schwarz and H. Hora (Springer US, Boston, MA, 1972) pp. 515–526.
- [15] S. V. Coggeshall and R. A. Axford, *Phys. Fluids* (1958-1988) **29**, 2398 (1986).
- [16] S. V. Coggeshall and J. Meyer-ter Vehn, *J. Math. Phys.* **33**, 3585 (1992).
- [17] S. V. Coggeshall, *Phys. Fluids A: Fluid Dynamics* (1989-1993) **3**, 757 (1991).
- [18] W. J. Krauser *et al.*, *Physics of Plasmas* **3**, 2084 (1996).
- [19] N. R. Morgan *et al.*, *Journal of Computational Physics* **259**, 568 (2014).
- [20] N. R. Morgan *et al.*, *Journal of Computational Physics* **290**, 239 (2015).
- [21] D. E. Burton *et al.*, *Journal of Computational Physics* **299**, 229 (2015).
- [22] D. E. Burton *et al.*, *Journal of Computational Physics* **355**, 492 (2018).
- [23] W. L. Oberkampf *et al.*, *Applied Mechanics Reviews* **57**, 345 (2004).
- [24] S. Chandrasekhar, *Communications on Pure and Applied Mathematics* **20**, 251 (1967).
- [25] L. Ovsyannikov, *Group Analysis of Differential Equations* (Elsevier Science, 2014).
- [26] L. Ovsyannikov, *Lectures on the Theory of Group Properties of Differential Equations* (World Scientific Publishing Company, 2013).
- [27] I. Nemchinov, *Journal of Applied Mathematics and Mechanics* **29**, 143 (1965).
- [28] S. Anisimov and I. Lysikov, *Journal of Applied Mathematics and Mechanics* **34**, 882 (1970).
- [29] F. J. Dyson, *Free Expansion of a Gas (II) Gaussian Model*, Tech. Rep. (1958).
- [30] F. J. Dyson, *Journal of Mathematics and Mechanics* **18**, 91 (1968).
- [31] T. Hara, T. Matsuda, and K. Nakazawa, *Progress of Theoretical Physics* **49**, 460 (1973).
- [32] Y. V. Tarasova, *Journal of Applied and Industrial Mathematics* **4**, 570 (2010).
- [33] S. Y. Shieh, *Journal of Mathematical Physics* **24**, 2438 (1983).
- [34] C. Rogers and W. K. Schief, *Nonlinearity* **24**, 3165 (2011).
- [35] B. Gaffet, *Journal of Fluid Mechanics* **325**, 113–144 (1996).
- [36] B. Gaffet, *Physica D: Nonlinear Phenomena* **132**, 233 (1999).
- [37] B. Gaffet, *Journal of Physics A: Mathematical and General* **33**, 3929 (2000).
- [38] B. Gaffet, *Journal of Physics A: Mathematical and General* **34**, 9195 (2001).
- [39] B. Gaffet, *Journal of Physics A: Mathematical and General* **34**, 2097 (2001).
- [40] B. Gaffet, *Journal of Physics A: Mathematical and General* **39**, 99 (2005).
- [41] B. Gaffet, *Journal of Physics A: Mathematical and Theoretical* **43**, 165207 (2010).
- [42] S. D. Ramsey, *The linear velocity profile class of hydrodynamics verification test problems*, Tech. Rep. LA-UR 11-02766 (Los Alamos National Laboratory, 2011).
- [43] S. V. Coggeshall, *Applications of Group-invariant Analytic Solutions to Internal Confinement Fusion*, Tech. Rep. LA-UR 92-2582 (Los Alamos National Laboratory, 1992).
- [44] S. V. Coggeshall, *Group-invariant Solutions of Hydrodynamics*, Tech. Rep. LA-UR 94-1277 (Los Alamos National Laboratory, 1994).
- [45] J. F. Giron *et al.*, *Phys. Rev. E* **101**, 053101 (2020).
- [46] J. McHardy *et al.*, *AIP Advances* **9**, 085113 (2019).
- [47] F. H. Harlow and A. A. Amsden, *Fluid dynamics: a LASL monograph (Mathematical solutions for problems in fluid dynamics)*, Tech. Rep. LA 4700 (Los Alamos National Laboratory, 1971).
- [48] F. Mandl, *Statistical Physics*, CIBA Foundation Symposium (Wiley, 1988).
- [49] R. Bowley and M. Sánchez, *Introductory Statistical Mechanics*, Oxford science publications (Clarendon Press, 1999).
- [50] C. Adkins and C. Adkins, *Equilibrium Thermodynamics* (Cambridge University Press, 1983).
- [51] L. Landau and E. Lifshitz, *Statistical Physics*, v. 5 (Elsevier Science, 2013).
- [52] M. Zemansky, M. Abbott, and H. Van Ness, *Basic engineering thermodynamics*, International student edition (McGraw-Hill, 1966).
- [53] R. A. Axford, *Laser and Particle Beams* **18**, 93 (2000).
- [54] S. V. Tsinopoulos *et al.*, *Journal of the Acoustical Society of America* **105**, 1517 (1999).
- [55] M. Spiegel, *Schaum's Outline of Theory and Problems of Vector Analysis and an Introduction to Tensor Analysis*, Schaum's outline series of theory and problems of vector analysis (Schaum Publishing Company, 1959).
- [56] R. C. Hendon and S. D. Ramsey, *Radiation Hydrodynamics Test Problems with Linear Velocity Profiles*, Tech. Rep. (Los Alamos National Lab.(LANL), Los Alamos, NM (United States), 2012).
- [57] Z. M. Boyd, E. M. Schmidt, S. D. Ramsey, and R. S.

Baty, The Quarterly Journal of Mechanics and Applied Mathematics **72**, 501 (2019).

[58] P. Sachdev and W. Janna, Appl. Mech. Rev. **54**, B108 (2001).